

Wave Propagation Through Random Media: Contributions from Ocean Acoustics

STANLEY M. FLATTÉ

Invited Paper

Abstract—Recent theoretical and experimental progress in understanding sound transmission through a random field of internal waves is reviewed. Some attempt is made to place this work in historical relation to similar efforts in radio-wave propagation through the ionosphere and light propagation through the atmosphere. It is emphasized that internal waves as a random medium possess several new features unfamiliar to those dealing with homogeneous isotropic turbulence. The effect of a background deterministic wave-speed variation (the ocean sound channel) is central to the theoretical treatment, which is based on a path-integral solution of the parabolic wave equation. A distinction is made between two sections of the saturated region, and some emphasis is placed on the region of partial saturation. Comparison with experiment is discussed with examples from the two-point mutual coherence function of time, frequency, and vertical separation; the intensity correlation in time, frequency, and vertical separation; the spectra of phase and log intensity, pulse propagation, and the higher moments of intensity.

I. INTRODUCTION

ACOUSTIC PROPAGATION in the ocean is an example of a more general branch of science; namely, wave propagation through random media (WPRM), the first reference to which may be that of Newton [1] who pointed out that even were the ultimate telescope to be designed, "yet there would be certain bounds beyond which telescopes could not perform. For the air through which we look upon the Stars is in a perpetual tremor; as may be seen by the tremulous motions of shadows cast from high towers, and by the twinkling of the fixed stars." Our understanding of this problem has gone far beyond Newton's solution, which was to ascend a mountain top. Instead, we attempt to quantitatively understand the limits that randomness imposes on the practical uses of wave propagation, we design signal forms that are robust against this randomness, and we use observations of wave fluctuations to probe the statistical, physical characteristics of different media. Progress in this field has involved coupling of the theory of WPRM with investigation into the detailed character of the (generally fluid) random medium. It is fair to say that essentially no progress has been made by anyone attempting a direct attack on the general theory without a deep physical understanding of a particular medium.

The modern theory of WPRM may be said to have begun in the late 1940's and early 1950's [2]–[4], when researchers used perturbation techniques to develop general formulas for propagation through weak fluctuations. In comparing with experiment, they assumed the medium was characterized by a Gaussian correlation function, but unfortunately, no natural medium is

known with this property. A major step forward was taken in the 1960's in response to developing understanding of Kolmogorov's pioneering characterization of the $p = 5/3$ power-law spectrum of homogeneous, isotropic turbulence (HIT). A theory for wave propagation through HIT was developed, primarily by Soviet workers, and successfully applied in the case of weak fluctuations to light transmission through the atmosphere. Their work was summarized in the influential book by Tatarskii [5] and a review article by Prokhorov *et al.* [6], and more recent results in this field are covered in the review articles by Ishimaru [7], Fante [8], and Tatarskii and Zavorotnyi [9], as well as in the book edited by Strohbehn [10]. After unsuccessful attempts to understand the case of strong fluctuations by use of Feynman diagram techniques, the basic theoretical method introduced in the late 1960's for strong fluctuations was the method of moment equations, wherein partial-differential equations are developed for the statistical moments of the propagating wave field. Although HIT may often be a good model for the atmospheric medium, one of the difficulties of treating light transmission through the atmosphere remains the assumption of HIT, which surely is not the main source of randomness in many situations.

The problem of radio-wave propagation in and through the earth's ionosphere has been of interest since the 1940's. This field made a crucial contribution to WPRM through the work of Leontovich and Fok [11], who introduced the parabolic-equation method, which treats waves that are concentrated within a small angular region around the direction of propagation. Nearly all subsequent work, including this review article, have used the parabolic equation as a starting point. The characterization of the ionospheric medium cannot rely on HIT; in particular, the medium is known to be anisotropic, and its power-law decay exponent is often different from $5/3$ [12], [13].

Interest in radio waves through interplanetary plasma was stimulated in the 1960's by increased activity in radio astronomy, and some of the first important results applicable when intensity fluctuations are large were obtained in the attack on this problem. In particular, Mercier [14] obtained a solution to the deeply modulated phase screen (wherein all fluctuations are concentrated at one range somewhere between source and receiver). Work on this problem has now had detailed treatment in the analysis of data from spacecraft radio transmission through the solar wind [15]–[17], and in occultation by planetary ionospheres [18]–[22]. These analyses have for the most part been restricted to the region of small intensity fluctuations, with the significant exception being use of the second moment for strong fluctuations [15], [16].

Work on fluctuations in sound transmission through the ocean during the 1960's was largely a misguided attempt to graft the

Manuscript received June 2, 1983; revised August 18, 1983. This work was supported in part by ONR, Code 4250A.

The author is with the La Jolla Institute Center for Studies of Nonlinear Dynamics, La Jolla, CA 92037; on leave from the University of California at Santa Cruz.

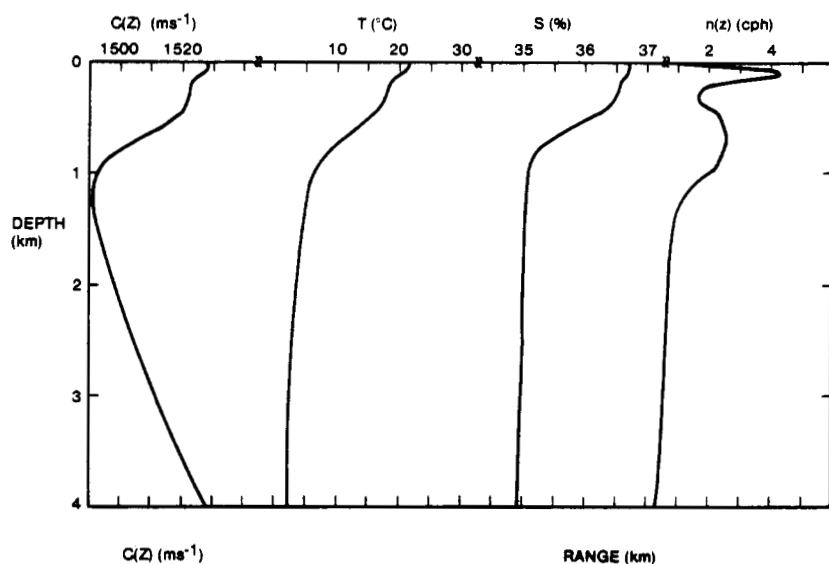


Fig. 1. Average, smoothed profiles of sound speed $C(z)$, temperature T , salinity S , and buoyancy frequency $n(z)$ as a function of ocean depth for a region of the Atlantic Ocean near Bermuda [32].

concept of HIT onto ocean variability [5]. By the mid 1970's oceanographers had identified internal waves as the most important source of variability on time scales from a few minutes to a day [23]. This new field of variability differs from HIT in five important ways. First, it is highly anisotropic, having vertical scales from 10 m to 1 km, and horizontal scales of 200 m to 20 km. Second, the connection between its spatial and temporal behavior is governed by the internal-wave dispersion relation rather than the usual HIT assumption: the Taylor hypothesis of frozen fluctuations advected by a mean wind. Third, the power law of its spectrum is approximately $p = 2$ rather than $p = 5/3$. Fourth, its strength is a strong function of ocean depth, typically being exponentially decreasing from the surface with a scale length of a few hundred meters. The fifth reason is even more unusual than the first four; that is, even in the absence of fluctuations, a ray from a source to a receiver is not a straight line; it is a curve controlled by a deterministic, depth-dependent, background variation in wave speed called the ocean sound channel (see Fig. 1).

This new medium provided a challenge to those interested in WPRM as applied to ocean acoustics. A significant response to this challenge was developed over the late 1970's by a group of scientists supported by DARPA, and later, ONR, and whose work as of 1978 is summarized in [24]. The first success in this area was achieved for weak fluctuations by Munk and Zachariasen [25], whose absolute calculations of variances in phase and log intensity from internal-wave effects were within a factor of two of the available experimental results. Strong fluctuations were another matter. The group felt that modifying the moment-equation method to account for any one of the just mentioned five differences was possible, but accounting simultaneously for all five was very difficult. Instead, the group returned to first principles in the form of the parabolic equation. At about this time Tappert [26], [27] introduced the idea of numerically solving the parabolic equation for deterministic ocean-acoustic problems. Some attempt was made to investigate the effect of fluctuations numerically on a realization-by-realization basis [28], but it was soon realized that analytical techniques would be essential. A method of solution based on Hamilton's principle was chosen.

Hamilton worked in the early 1800's on the propagation of

light, at a time when Newton's corpuscular theory was still in ascendance; he successfully found the general method for determining the path of a particle through an arbitrary potential from a variational principle. That is, he considered all possible paths for the particle, and, by the principle of stationary action, determined the true path. Although Hamilton himself, seeing the successes of the wave theory of light by the 1830's, stated that his method could be used for wave as well as particle propagation [29], it was not until the 1940's that it was quantitatively realized, by Feynman [30], that Hamilton's principle could be used to solve a full parabolic wave equation (the Schrodinger equation of quantum mechanics), where the arbitrary potential corresponds to an arbitrary field of wave speed. Instead of searching for the one true particle path, Feynman added all possible paths together, each path having a phase factor given by ϵA , where ϵ is a constant and A is the action. This is the *path integral*. In the case of quantum mechanics, ϵ is $1/h$, while in WPRM, it is proportional to the wavenumber of the propagating wave. As $\epsilon \rightarrow 0$, the full path integral is dominated by paths infinitesimally close to the path of stationary action, and can be solved by stationary phase. For finite ϵ , the result of the path integral is the complete wavefunction.

The basic step forward in the theory of WPRM that took place between 1975 and 1977 was the consideration of the arbitrary field of wave speed in Feynman's path integral as a statistical random medium [24], [31]. This step, in combination with the understanding of the ocean internal-wave field as the source of medium fluctuations, led to comparisons with a number of ocean acoustics experiments [24], [32]–[34], whose results will be discussed later in this review.

This step forward was taken in order to deal with the five complications mentioned, all of which apply to ocean acoustics. The results obtained with the path-integral technique are useful for cases where these five complications do not all pertain, such as those which occur in electromagnetic propagation. In particular, it has been known for a long time that the theory of WPRM, when the parabolic equation is valid, is essentially complete as long as the intensity fluctuations are small compared with unity. In the past, major theoretical difficulties arose if the variance of normalized intensity (the scintillation index) is comparable to

unity. The first experimental observation of the disagreement [35] showed that the scintillation index saturated around unity as the propagation range or the strength of medium fluctuations became large. The first rather unsuccessful attempts to deal with the physics implied by this phenomenon involved diagram techniques [5], with other work involving the cluster approximation [36], [37]. Although the path-integral method provides a simple, more general derivation for many results when the intensity fluctuations are small (unsaturated), its power is most evident in the saturated region, as will be seen in the following. It is of interest to note that work on the saturated region for the atmospheric optics case is now dominated by the path-integral technique [9], although understandably that community has not grappled with the difficulties of curved equilibrium rays, nor with the special character of internal-wave fluctuations.

Successes of the path-integral method in ocean acoustics, to be described in the following, include increased understanding of the time and space behavior of the complex wave function; quantitative calculations of the mutual coherence function as a function of separations in time, vertical position, and horizontal position; the spectra of phase, intensity, and log intensity; behavior of pulse propagation; and some results on the higher moments of intensity that provide some understanding of the intensity probability density distribution. These results are mostly first corrections to asymptotic behavior, and hence have a region of validity that is not complete. Comparisons with experiment have been made for acoustic frequencies between 200 Hz and 13 kHz, and for propagation ranges between 20 and 1300 km.

The major unsolved problems of WPRM in ocean acoustics are the following. First, the model of medium fluctuations as dominated by internal waves with a particular empirical spectrum [23] will not be universally valid in all ocean regions, and will not be appropriate for very-high-frequency (> 20 -kHz) propagation, where ocean processes (microstructure) with scales smaller than internal waves will probably dominate. Second, both the unsaturated and saturated theories are asymptotic in the sense that their results are not expected to apply at or near the boundary between them where the scintillation index is first becoming comparable to unity. Some success in this area has been achieved at the expense of ignoring the effect of the sound channel, as well as assuming a Gaussian correlation function for the medium [38], or using certain mathematical approximations [39]. Third, curved rays give rise to caustics, even in the absence of medium fluctuations, and the present theory fails near caustics. Some work on the intensity near caustics has been done [40]. Attempts [41], [42] have been made to deal with the deterministic caustic problem in the context of the second-moment equation; they have either verified the asymptotic path-integral result or have led to methods requiring extensive numerical computation. Fourth, given a level of inhomogeneity and anisotropy, the present fluctuation theory is inadequate below some low acoustic frequency (for internal-wave-induced fluctuations this occurs for frequencies in the range of 10–100 Hz). Treatments of the highly anisotropic case have been given [43], [44] for application to these low frequencies. Treatments of a general value of anisotropy and inhomogeneity still require extensive computation. Fifth, the limitations on experimental separation of the deterministic sound channel from the sound-speed fluctuations are substantial because of the red spectrum of the fluctuations. Those acoustics properties that are sensitive to the second derivative of the sound channel are particularly difficult to calculate reliably [32]–[34]. Furthermore, if simple ray theory is not applicable in the absence of fluctuations, such as occurs when the deterministic sound-speed

profile changes rapidly within a Fresnel zone (e.g., some ocean surface ducts), then significant new problems arise. Useful techniques based on ideas of radiative transport theory have been developed [45]–[47] in part for this problem.

This review begins with a short description of the ocean sound channel responsible for curved deterministic rays (see Section II-A), in which nomenclature for quantities related to the Fresnel zone are introduced (Section II-B). There follows a description of the ocean internal-wave field (Sections II-C–E). Section III describes the path integral and its results from a physical point of view, and introduces the Λ – Φ diagram on which are placed the various transmission regions (e.g., unsaturated and saturated). Section IV briefly covers the moment-equation method, and compares it to the path integral. Results for the coherence of the complex wavefield (two-point function, or second moment), the coherence of intensity (four-point function, or fourth moment), and the probability density function (PDF) of intensity (moments higher than fourth) are presented in Sections V–VII. Phase and log-amplitude fluctuations, of such practical interest in so many situations, are treated in Section VIII.

This review considers only a small fraction of the topics of interest in WPRM. The propagating wave amplitude is assumed to be infinitesimal, so that no finite-amplitude, nonlinear effects such as shock waves arise. The fluctuations in wave propagation are assumed to arise from variations in wave speed on scales large compared with a propagating wavelength; no Bragg scattering, or backscattering, or scattering off particulates of various kinds, occurs. The medium is treated as continuous; no scattering from specifically shaped regions (even though they might be distributed in a random fashion) is considered. No boundary scattering is considered, such as would occur at the surface or bottom of the ocean. The medium is considered to have a large extent transverse to the direction of propagation; if this were not the case (e.g., in shallow-water low-frequency ocean acoustics) then normal-mode theory would be preferable to the ray-based theories discussed here. Likewise, the sound channel is assumed to be a smooth function of depth; in cases where the sound channel has sharp variation within an acoustic wavelength (e.g., strong ocean surface ducts) again ray-based theories have difficulties. The source is taken to be a point. Although this is not a limitation in principle, no explicit treatment of finite-sized collimated beams will be given here. Investigations of a number of the previously mentioned difficulties lead into fields with a large and rich literature which we have not attempted to summarize in this review. Despite these limitations, the resulting problem is realistic, and it is difficult because of its nonlinearity in the strength of the medium fluctuation, which appears in a multiplicative fashion in the partial-differential equation for the propagating wave field.

II. OCEAN ACOUSTIC PROPERTIES

A. The Sound Channel

The most striking feature of ray propagation in the ocean is the sound channel, discovered by Ewing and Worzel [48]. The sound-speed profile has a minimum at a depth that varies with geographical location, but is typically about 1 km. Rays tend to bend toward regions of smaller sound speed, and are thereby *channeled* toward the depth of minimum speed, called the sound axis. As a result, refracted rays may extend for thousands of kilometers in range, never touching surface or bottom.

The typical sound-speed profile (Fig. 1) is a result of the competition between the stratification of the ocean (in temper-

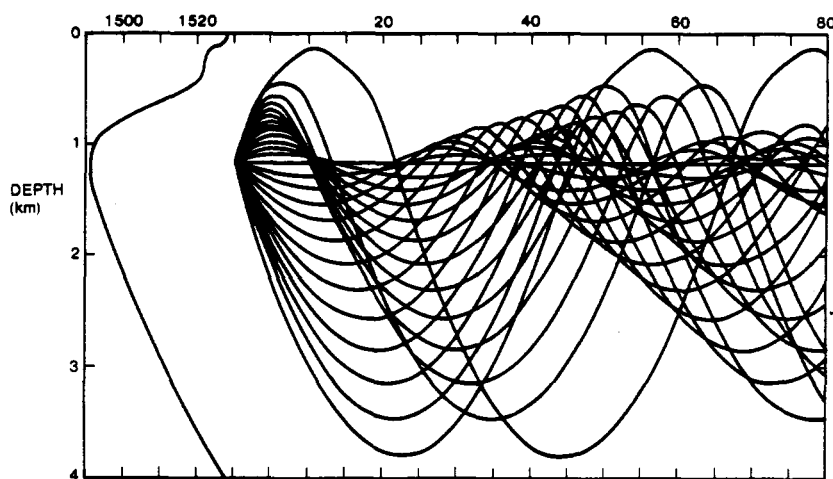


Fig. 2. Rays from a source on the sound axis for the sound-speed profile of Fig. 1. Caustics and shadow zones are clearly evident.

ature and salinity) which tends to give a sound-speed decrease with depth, and the adiabatic pressure gradient, which tends to give an increase with depth. The stratification dominates in the upper regions and the pressure gradient dominates in the lower depths.

In the geometrical-optics approximation, the field transmitted from a source can be described completely in terms of rays, whose characteristics are determined by the sound speed as a function of position. The frequency of sound σ enters only to the extent that the phase along a ray varies in a simple manner according to $\varphi = \int [\sigma/C(z)] ds$ where ds is the element of path length, $C(z)$ is the local sound speed, and z is the vertical coordinate measured upward from the ocean surface. (The symbol ω will be reserved for internal-wave frequency.)

The general equation of ray optics for a ray in a depth-dependent sound-speed profile may be expressed as

$$\partial_x \vartheta = -C^{-1} \partial_z C \quad (1)$$

where ϑ is the angle of the ray with the horizontal x coordinate and $\partial_x z = \tan \vartheta$. Equation (1) is a generalized Snell's law, derived from the eikonal equation. It may be used to numerically integrate a ray from any initial starting depth and angle. Since $\partial_z C$ is positive above the sound axis and negative below the sound axis, a general result of (1) is that the rays always bend toward the sound axis. This is the principle of the *sound channel*.

Fig. 2 shows a set of rays from a source on the sound axis propagating to a range of 80 km. After a few tens of kilometers, the sound field has a rather complicated structure. Several rays from a single source may arrive at a receiver from different directions, giving rise to *multipath*. Regions exist through which no rays pass (shadow zones). Envelopes to families of rays exist, called caustics. These effects have been extensively studied (e.g., [49]). Fig. 3 shows a typical ray with some of its parameters defined.

Because the sound speed $C(z)$ never varies by more than a few percent from the reference C_0 , fully refracted rays within the ocean volume never attain angles of more than $\approx 15^\circ$ from the horizontal, a fact important to the parabolic-equation approximation. In the ray approximation, this is equivalent to setting $\tan \vartheta = \vartheta$; we may then replace (1) by

$$\partial_{xx} z = -C^{-1} \partial_z C. \quad (2)$$

Defining a dimensionless function $U_0(z)$ by

$$C(z) = C_0 [1 + U_0(z)] \quad (3)$$

we have, for small $U_0(z)$,

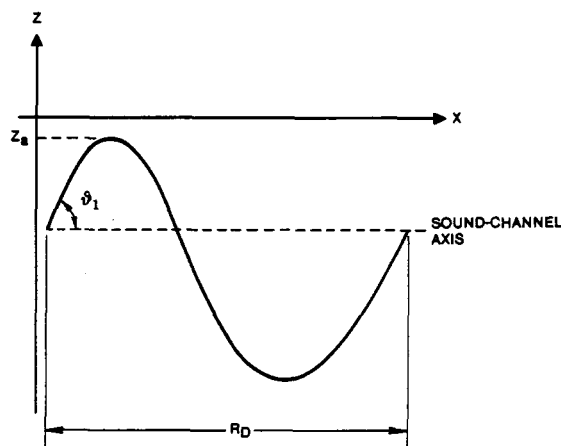


Fig. 3. Any ray in a range-independent environment is characterized by the parameters of its double loop. The sound-channel axis is at the depth where $U'(z) = 0$. The depth of the upper turning point is z_a , the double-loop length is R_D , and the ray angle at the axis is ϑ_1 .

$$\partial_{xx} z = -U'_0(z) \quad (4)$$

so that ray geometry is controlled by the first derivative of U_0 .

B. Ray Tubes, the Green's Function, and the Fresnel Zone

In addition to the geometry of a single ray, the dimensions of a *ray tube* will enter in an essential way into the WPRM theory. In the first place, the ray-tube cross section determines ray intensity in the geometrical optics approximation.

More importantly, approximate evaluation of a number of path integrals yields results in terms of ray tubes. For example, the wavefunction coherence between two points separated vertically will involve a ray tube from the source to those two points (Fig. 4(a)). A number of fluctuation effects will depend upon the relation between two ray tubes, one from the source and one from the receiver (Fig. 4(b)), whose behavior is determined by a Green's function. Finally, a particularly important aspect of ray tubes is the Fresnel zone, which is a function of position along the ray, and which can be evaluated by use of the Green's function (Fig. 4(b)). It should be emphasized that ray-tube behavior is determined by the behavior of the second derivative of U_0 (see the following) and the source-receiver geometry; the relation to fluctuation quantities will be discussed in more detail later.

Consider a ray tube, consisting of nearby rays surrounding the unperturbed ray. The differential equation satisfied by rays $z(x)$

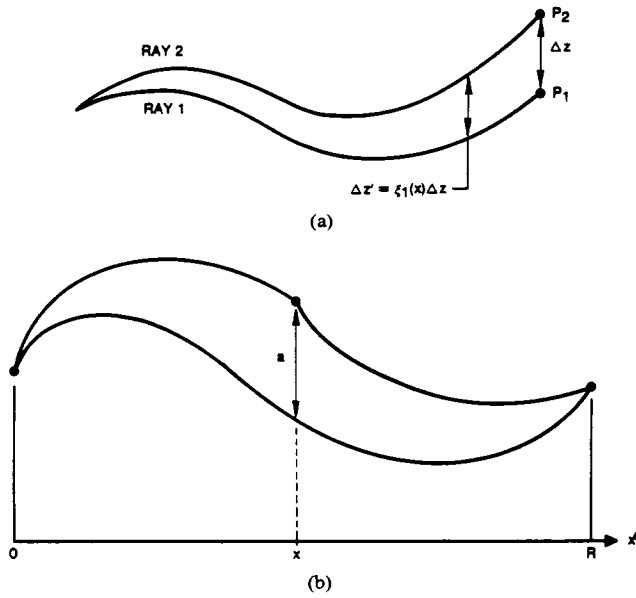


Fig. 4. Geometry of curved rays in a deterministic sound-speed profile. (a) The separation of two rays emanating from one source is a complicated function of range x , but to first approximation can be expressed as a ray-tube function $\xi_1(x)$ times the separation at range R . (b) The Fresnel zone size is the value of a such that the broken ray is $\lambda/2$ longer than the unbroken ray, where λ is the transmitted wave frequency.

close to the original ray $z_{\text{ray}}(x)$ where

$$z(x) = z_{\text{ray}}(x) + \xi(x) \quad (5)$$

is, for small $\xi(x)$,

$$\partial_{xx}\xi(x) + U_0''\xi(x) = 0. \quad (6)$$

Hence properties of ray tubes are controlled by U_0'' . Solutions to (6) can be defined as $\xi_1(x)$, $\xi_2(x)$, and $S_1(x)$ where

$$\begin{aligned} S_1(0) &= \xi_1(0) = \xi_2(R) = 0 \\ \xi_1(R) &= \xi_2(0) = 1 \\ S_1'(0) &= 1. \end{aligned} \quad (7)$$

For example, a ray tube originating at the source and terminating at two points separated vertically by Δz would have vertical extent $\xi_1(x)\Delta z$ (Fig. 4(a)).

Consider a ray tube consisting of an unbroken ray from source to receiver and a second ray broken at range x (Fig. 4(b)). This could also be considered as two ray tubes meeting at x . The Green's function $g(x, x')$ is used to represent this situation, normalized so that the broken ray has a discontinuity in derivative of unity. Thus we have

$$\partial_{x'x}g(x, x') + U_0''g(x, x') = \delta(x' - x) \quad (8)$$

with $g(x, 0) = g(x, R) = 0$. The solution for $g(x, x')$ can be given in terms of the ray tube functions as

$$g(x, x') = \begin{cases} \xi_1(x')\xi_2(x)S_1(R), & \text{on } (0, x) \\ \xi_1(x)\xi_2(x')S_1(R), & \text{on } (x, R). \end{cases} \quad (9)$$

It turns out that the well-defined function $g(x, x')$ is related to the Fresnel zone. Let the acoustic path length difference between the equilibrium ray and the broken ray in Fig. 4(b) be $S(a)$. It can be shown [24] that for infinitesimal a

$$S(a) = \frac{1}{2} \frac{a^2}{g(x, x)}. \quad (10)$$

The radius of the first Fresnel zone (R_F) is defined by

$$S(R_F) = \frac{\lambda}{2} \quad (11)$$

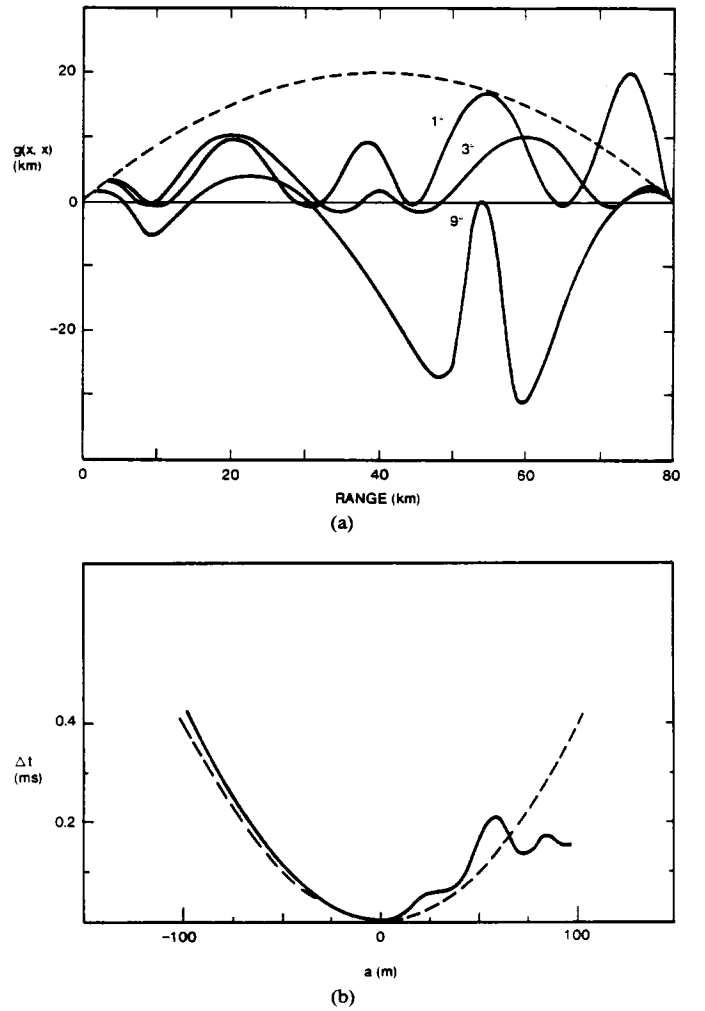


Fig. 5. The Green's function which appears in the definition of the Fresnel zone: $R_F^2 = \lambda g(x, x')$. (a) Examples of $g(x, x')$ for three rays from Fig. 2, for a range of 80 km. The dashed line is $g(x, x')$ for a straight-line ray without a sound channel. (b) The solid curve is a numerical calculation of $S(a)$ for an empirical $c(z)$ profile. The dashed parabola is the quadratic approximation to $S(a)$ that the value of $g(x, x')$ would predict for this case.

where λ is the acoustic wavelength. So that

$$R_F(x) = [\lambda g(x, x')]^{1/2}. \quad (12)$$

Thus the Fresnel zone is closely related to the Green's function. The *phase curvature* function $A(x)$, defined in [24] is perhaps better given as its equivalent, $g^{-1}(x, x')$. It is important to note that at finite values of λ the validity of (10) will only be approximate. Only preliminary investigations of this approximation have been made [34]. Note that one can write

$$g(x, x') = \begin{cases} \frac{\xi_1(x')}{\xi_1(x)} g(x, x), & \text{on } (0, x) \\ \frac{\xi_2(x')}{\xi_2(x)} g(x, x), & \text{on } (x, R). \end{cases} \quad (13)$$

Some specific examples of ray tube functions can now be given. For no background sound channel (homogeneous group velocity or linear velocity profile), where $U_0'' = 0$, we obtain

$$g(x, x') = \begin{cases} \frac{x'(R-x)}{R}, & \text{on } (0, x) \\ \frac{x(R-x')}{R}, & \text{on } (x, R) \end{cases} \quad (14)$$

which gives (Fig. 5)

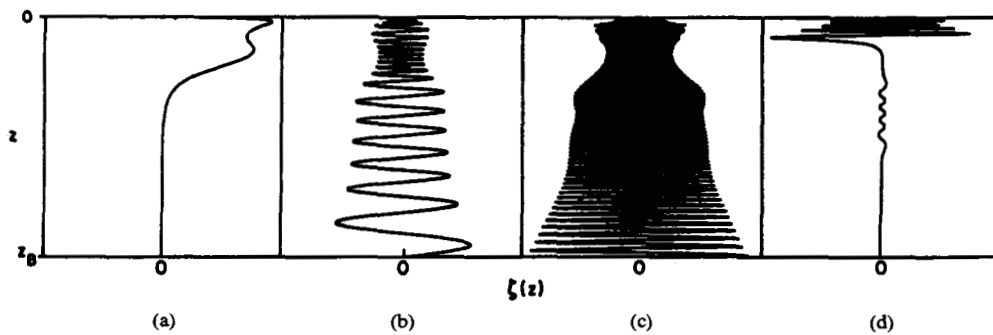


Fig. 6. Some shapes of the vertical eigenfunction $W(z)$ for internal waves in waters of the Bermuda experiment: for $k = 0.5$ cycle/km, mode $j = 1$ (a), 40 (b), and 250 (c). To illustrate vertical trapping of modes, (d) shows $j = 40$, $k = 10$ cycles/km.

$$g(x, x) = \frac{x(R-x)}{R}. \quad (15)$$

For the parabolic channel with near-axis rays, U_0'' is a constant. The solutions to (6) will be sines and cosines. Define $2\pi/K$ to be the wavelength of the sinusoidal ray, which is the range of the double axis loop; we can see $K = (U_0'')^{1/2}$. We obtain

$$g(x, x') = \begin{cases} \frac{\sin Kx' \sin K(R-x)}{K \sin KR}, & \text{on } (0, x) \\ \frac{\sin Kx \sin K(R-x')}{K \sin KR}, & \text{on } (x, R) \end{cases} \quad (16)$$

which gives

$$g(x, x) = \frac{\sin Kx \sin K(R-x)}{K \sin KR}. \quad (17)$$

Difficulties arise when $g(x, x)$ goes through infinity, which is a caustic. This happens when $S_1(R) = 0$ so that the boundary conditions cannot be satisfied.

Avoiding caustics, we can define a ray tube by means of $g(x, x)$, in such a way that all paths within a ray tube have an (optical or acoustic) path length within $\lambda/2$ of each other. An example for a realistic sound channel is shown in Fig. 5. It should be remarked here that a major limitation on present ability to compare theory and experiment in ocean acoustics is the difficulty of determining U_0'' in the presence of small-scale random structure such as internal waves. There is not a sufficiently clear-cut scale separation in either spatial or temporal frequency. Furthermore, since (10) is only approximate, the estimate (12) for R_F is not exact for finite λ even if U_0'' is known exactly. Fig. 5 shows a numerical evaluation of $S(a)$ compared with the quadratic approximation (10) for an observed profile.

C. Internal Waves

The ocean is not uniform in density, principally because its surface is heated near the equator by the sun, and freshened near the poles by ice. This stratification is mostly stable, such that deeper water is denser. The variation of density is on the order of 0.1 percent from the top to bottom of the ocean. Dynamic disturbances such as surface waves, currents flowing over bottom topography, or nonlinear dynamical interactions within the volume of the ocean can create waves within this stratification, much as wind creates waves on that density interface that is the ocean surface.

The behavior of internal waves is controlled by the density gradient, given in the useful form of the buoyancy frequency

$$n(z) = \left\{ -\frac{g}{\rho} \partial_z \rho \right\}^{1/2} \quad (18)$$

where ρ is potential density and g is the acceleration of gravity. (The difference between potential and actual density gradient is the adiabatic gradient due to the pressure effect.) A parcel of water, if displaced vertically from its equilibrium position, would oscillate with this frequency if not subjected to forces other than that of static buoyancy. An internal wave displacement field may be decomposed into a horizontally traveling waves. Let the displacement ζ of an isodensity surface at position x and time t be decomposed into waves of the form

$$\zeta(x, t) = W(z) \exp \{ i(kx - \omega t) \}. \quad (19)$$

One boundary condition on $W(z)$ is $W(-h) = 0$ where h is the depth of the ocean. The free surface boundary condition at $z = 0$ is more complicated, but is very well approximated by $W(0) = 0$ [50]. Thus internal waves in the ocean behave as though in a fluid with a rigid, flat bottom and top.

The equation that $W(z)$ must satisfy comes from the usual linearized equations of fluid dynamics and is [24]

$$\partial_{zz} W + \left(\frac{n^2(z) - \omega^2}{\omega^2 - \omega_i^2} \right) k^2 W = 0 \quad (20)$$

where ω_i represents the effect of the rotation of the earth and is called the inertial frequency

$$\omega_i = 2\Omega \sin(\text{lat}) \quad (21)$$

where Ω is the earth's rotation rate and lat is the latitude. The solutions to (20) can be given in terms of eigenfunctions. The behavior of these eigenfunctions (Fig. 6) can be as complicated as the profile of $n(z)$, but in general the modes, labeled by j , have $j-1$ nodes.

The phase speed of internal waves is crucial to understanding the relationship between spatial and temporal variability in the ocean. The phase speed is obtained from the dispersion relation, which for low modes is complicated to calculate, but which for high modes can be found from a WKBJ approximation where slowly varying $n(z)$ is assumed [51]. The result is

$$k \approx \frac{\left(j - \frac{1}{4} \right) \pi (\omega^2 - \omega_i^2)^{1/2}}{\int_{-h}^0 [n^2(z) - \omega^2]^{1/2} dz} \quad (22)$$

$$k_v \approx \frac{\left(j - \frac{1}{4} \right) \pi (n^2 - \omega^2)^{1/2}}{\int_{-h}^0 [n^2(z) - \omega^2]^{1/2} dz} \quad (23)$$

where the integral is taken over the range(s) of z in which the eigenfrequency ω is less than the local $n(z)$. Each mode may have any frequency between ω_i and n_{\max} (the maximum buoyancy

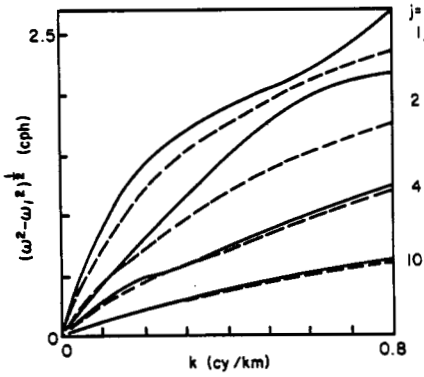


Fig. 7. Dispersion relations for the Bermuda experiment. Solid lines are numerical solutions to (20). Dashed lines are from (22).

frequency). For frequencies well below $n(z)$, the integral in (22) and (23) is commonly approximated by a constant called $n_0 B$. Thus

$$k \approx \frac{\left(j - \frac{1}{4}\right) \pi (\omega^2 - \omega_i^2)^{1/2}}{n_0 B}$$

$$k_\nu \approx \frac{\left(j - \frac{1}{4}\right) \pi n(z)}{n_0 B}. \quad (24)$$

Fig. 7 shows some dispersion curves for a typical Atlantic profile.

Thus internal waves move through the ocean with speeds of about $1 \text{ m} \cdot \text{s}^{-1}$ or less, with vertical wavelengths of a few kilometers or less, with frequencies between 1 cycle per day and a few cycles per hour, and with unrestricted horizontal wavelength. The next subsection discusses the distribution of energy actually observed among ocean internal waves.

D. The Internal-Wave Spectrum

Observations of ocean structure in temperature and salinity have been recorded for nearly 100 years. A picture is now built up of internal waves filling the world's oceans, with vertical displacements of approximately 10 m within 1 km of the surface, and with vertical (horizontal) wavelength ranging downward from 1 km (50 km). This field of waves has a vertically integrated average energy of approximately 0.4 J/cm^2 , not very different from the average energy density for surface waves.

Consider a random field $\mu(x, t)$ of internal-wave fractional sound-speed fluctuations. Thus the sound speed can be expressed as

$$C(x, t) = C_0[1 + U_0(z) + \mu(x, t)]. \quad (25)$$

The contributions to μ include fluctuations of temperature and salinity, and would in principle also include fluctuations in water velocity because of a Doppler shift. The water-velocity effect is about 10 percent of the temperature and salinity effect, so we will ignore it for the rest of this section [24] (but see Section V-D). Since μ is a random variable (with zero mean) we may define its correlation function

$$\rho(\Delta x, \Delta t; z) = \langle \mu(x, t) \mu(x', t') \rangle \quad (26)$$

with $\Delta x = x' - x$, $\Delta t = t' - t$, and where z is the average z coordinate of x and x' , indicating the possible inhomogeneous dependence on depth of ρ . Such a field can always be decomposed into its Fourier components, in both space (to generate a wave-vector distribution) and time (to generate a frequency distribution for each wave vector). Each wave-vector frequency

combination has an amplitude $A(k, \omega)$ associated with it for each realization of the random field. Hence

$$\mu(x, t) = \sum_{k, \omega} A(k, \omega) \exp \{i(k \cdot x - \omega t)\}. \quad (27)$$

We follow the usual hypothesis that the amplitudes are Gaussian random variables with zero mean, and independent of each other; that is, we may write

$$\langle A(k, \omega) \rangle = 0 \quad (28)$$

$$\langle A^*(k, \omega) A(k', \omega') \rangle = S(k, \omega) \delta_{kk'} \delta_{\omega\omega'} \quad (29)$$

where $S(k, \omega)$ is called the *spectrum* of sound-speed fluctuation. We may think of this spectrum as a decomposition of the fluctuation field into traveling waves, but, in fact, the above formulation can be used for any random field.

The spectrum of oceanic internal waves has four important general features:

1) Vertical confinement—The boundary conditions at top and bottom require that only standing waves (and hence modes) are present in the vertical component. This assumption need not be made; the spectrum can easily be modified if this assumption is relaxed.

2) Vertical inhomogeneity—Because of nonuniform stratification, the vertical eigenmodes of internal waves are not sinusoidal. However, the WKBJ approximation to the eigenfunctions can be made, yielding *locally* sinusoidal functions with amplitudes that vary with depth. Under this approximation, the only effect of vertical inhomogeneity is to cause a slow variation in $S(k, \omega)$, which we denote by $S(k, \omega; z)$.

3) Horizontal isotropy—The spectrum depends only on $k = (k_x^2 + k_y^2)^{1/2}$, and not k_x and k_y separately; $S(k, \omega; z) = S(k, k_\nu, \omega; z)$, where k_ν is the vertical (z) component of the wave vector.

4) Factorization—The spectrum is a function of three variables: k , k_ν , and ω ; or better: k , j , and ω , but only two of the three are independent if the dispersion relation (22) is valid. Empirically, internal-wave observations have been fit to a form which is a product of functions of ω and j as follows [23]:

$$S(\omega, j; z) = \langle \mu^2(z) \rangle N_\omega \frac{\omega_i (\omega^2 - \omega_i^2)^{1/2}}{\omega^3} \frac{N_j}{j^2 + j_*^2}, \quad \omega_i < \omega < n(z). \quad (30)$$

Thus at high ω or j , the spectrum has an inverse-square power law. The quantities N_ω and N_j are normalization constants such that the integral over ω and the summation over j of S yields $\langle \mu^2(z) \rangle$, the variance of internal-wave sound-speed fluctuation as a function of depth. For consistency with the WKBJ approximation to the mode vertical wavefunction, one can write [52]

$$\langle \mu^2(z) \rangle = \xi_a^2 \frac{n_a}{n(z)} (C^{-1} \partial_z C - \gamma_A)^2 \quad (31)$$

where ξ_a is the rms displacement of internal waves at a depth where $n(z) = n_a$. The adiabatic sound-speed gradient γ_A is typically $1.1 \times 10^{-4} \text{ km}^{-1}$. Values for ξ_a in the ocean are in the range of 2–20 m at $n_a = 3$ cycles/h (cph) and $j_* = 3$.

E. Acoustic Fluctuation Parameters

Certain functions of the random medium are crucial to the calculation of wave-propagation fluctuations. In this section we define the most important of these as Φ , the strength parameter; Λ , the diffraction parameter; and D , the phase structure function. The only properties of the propagating wave that enter into

these definitions are the wavenumber q and the existence of meaningful rays in the absence of medium fluctuations.

The character of the fluctuations in a wave field is given by two parameters corresponding to the *strength* and *size* of the time-dependent inhomogeneities. The strength of the fluctuations can be expressed as

$$\Phi^2 \equiv \left\langle \left(q \int \mu ds \right)^2 \right\rangle \quad (32)$$

where q is a reference wavenumber given by $q = \sigma/C_0$, and σ is the acoustic frequency. Equation (32) is the fundamental definition of Φ . It is of interest that an approximate value of ϕ can be obtained from

$$\Phi^2 \approx q^2 \int_0^R dx \int_0^R dx' \rho(x, x') \approx q^2 \int_0^R dx \langle \mu^2(z_{\text{ray}}) \rangle L_p(\vartheta, z_{\text{ray}}) \quad (33)$$

where x and x' are evaluated along the ray. L_p is a local correlation length along the ray defined by approximating the inner integral by a straight line tangent to the ray at x ; it can be evaluated for internal waves [53]. Thus Φ^2 is the integral along the equilibrium ray of a function involving internal-wave parameters.

The phase structure function is given by

$$D(1,2) \equiv \left\langle \left[\frac{\sigma_1}{C_0} \int_1 \mu ds - \frac{\sigma_2}{C_0} \int_2 \mu ds \right]^2 \right\rangle \quad (34)$$

where the labels 1 and 2 represent rays to different points, possibly at different frequencies.

$D(1,2)$ can also be expressed as an integral along the ray

$$D(1,2) \approx 2q^2 \int_0^R dx \langle \mu^2(z_{\text{ray}}) \rangle L_p(\vartheta, z_{\text{ray}}) f(\Delta; \vartheta, z) \quad (35)$$

where Δ is a general separation between rays 1 and 2; $f(\Delta; \vartheta, z)$ is the phase correlation function calculable from internal wave parameters [52]. For $\Delta = \Delta z$, a small vertical separation, it has been shown [52] that if $\Delta z \leq L_V/2$

$$f(\Delta z; \vartheta, z) \approx \frac{1}{2} \left(\frac{\Delta z}{L_V} \right)^2 \ln \left[\frac{L_V}{\Delta z} \right] \quad (36)$$

where $L_V = 0.74 n_0 B / n(z)$; this provides a definition of the vertical correlation length L_V .

The diffraction parameter is a weighted average along the ray of $(R_F/L_V)^2/2\pi$, where R_F is the Fresnel zone radius and L_V is the vertical correlation length. This quantity is given by

$$\Lambda \equiv \frac{q^2}{\Phi^2} \int_0^R dx \langle \mu^2(z_{\text{ray}}) \rangle L_p(\vartheta, z_{\text{ray}}) |g(x, x)| / q L_V^2. \quad (37)$$

Thus Λ is defined from the start as an integral along the equilibrium ray.

III. THE PATH INTEGRAL

The basic expression to be solved in WPRM is the wave equation

$$\partial_{tt}\varphi - C^2 \nabla^2 \varphi = 0. \quad (38)$$

In the parabolic approximation [11] one tries a solution of the form $\varphi = r^{-1/2} e^{i(qr - \sigma t)} \Psi(r, t)$ and neglects second-order derivatives in the x direction as well as any time derivatives of Ψ . The result is

$$2iq\partial_x \Psi = \{-\partial_{yy} - \partial_{zz} + 2q^2[U_0 + \mu(x, t)]\} \Psi. \quad (39)$$

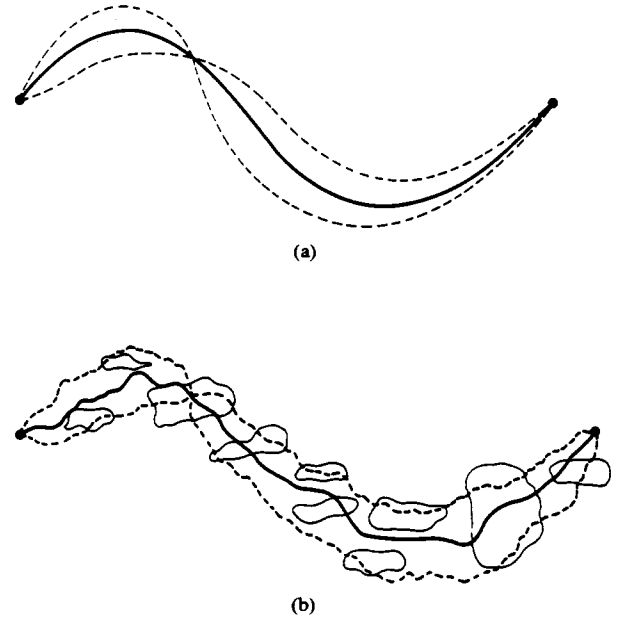


Fig. 8. The unsaturated region. (a) In the absence of random fluctuations there exists an equilibrium ray with its associated bundle of paths bounded approximately by a ray tube whose size is the Fresnel zone. (b) For weak fluctuations, the ray is perturbed in direction and travel time.

Physically, the neglect of second-order x derivatives corresponds to a small-angle approximation; that is, the propagating wavefront undergoes small-angle deviations while it travels a distance of one medium correlation length. The neglect of time derivatives of Ψ corresponds to a frozen-medium approximation. Typical ocean internal waves have phase speeds of less than $1 \text{ m} \cdot \text{s}^{-1}$, compared with $1500 \text{ m} \cdot \text{s}^{-1}$ for the speed of sound. The internal-wave medium can be regarded as frozen during the passage of the sound wave.

Equation (39) is a Schrödinger equation, and thus its solution can be directly expressed in terms of a path integral (see Feynman and Hibbs [30] for a detailed discussion of the path integral)

$$\Psi = N \int d(\text{path})$$

$$\cdot \exp \left[iqS_0(\text{path}) - iq \int_0^R \mu[x, y(x), z(x), t] dx \right] \quad (40)$$

where the integration is over all paths $[y(x), z(x)]$ connecting the source to the receiver. The unperturbed phase associated with the path is

$$qS_0 = q \int_0^R \left[\frac{1}{2} (\partial_x y)^2 - \frac{1}{2} (\partial_x z)^2 - U_0(z) \right] dx \quad (41)$$

and N is a normalization factor chosen so that $\Psi = 1$ for $\mu = 0$.

A. Qualitative Discussion

Consider the case in which $\mu = 0$. It is assumed that the evaluation of Ψ can be done by stationary phase, yielding the "equilibrium" ray(s). The paths that contribute to this result are those within a Fresnel zone of the equilibrium ray (Fig. 8(a)). Imagine that the fluctuations μ are very weak in some sense to be defined later. The contributions to Ψ still have only one stationary-phase ray which is dominant, although this ray and its associated ray tube are perturbed by the fluctuations (Fig. 8(b)). This condition is labeled unsaturated because the intensity fluctuations, due to the divergence or convergence of the ray

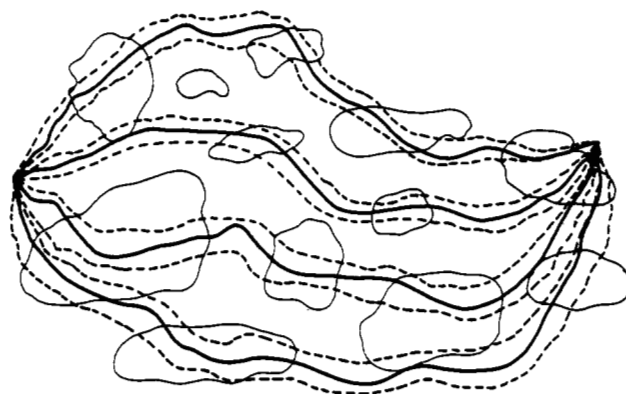


Fig. 9. The saturated region. For strong fluctuations, one equilibrium ray splits into many microrays.

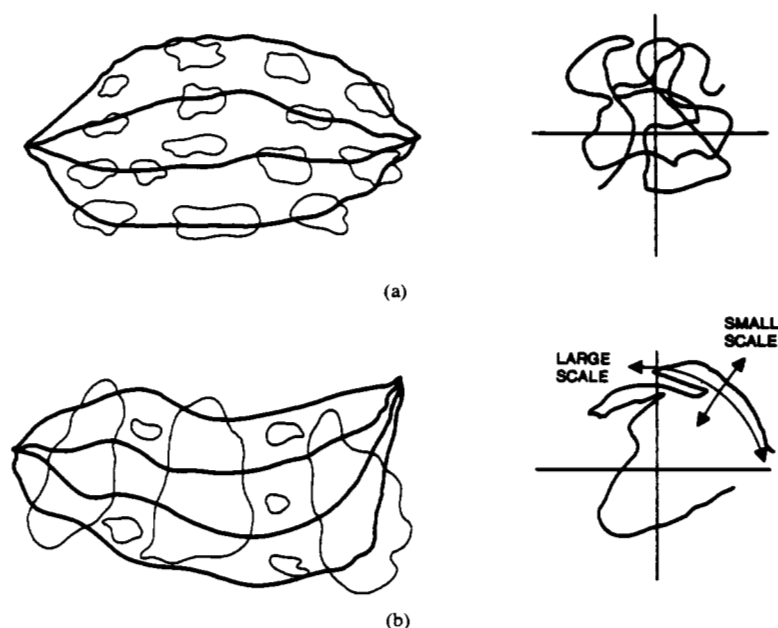


Fig. 10. The two regimes of the saturated region. (a) Full saturation: the microrays are separated by more than a correlation length resulting in a phasor composed of many independent complex amplitudes that execute a two-dimensional random walk. (b) Partial saturation: in a multiscale medium the small scale can create the microrays and resulting intensity fluctuations, while the large scales correlate a large number of microrays, thus affecting the overall phase.

tube, grow with μ or range. Now let the fluctuations μ become stronger. The Ψ function is now a sum of contributions from many rays (microrays) that have been created by the fluctuations. This condition is called saturated, because the intensity variance, now due mainly to the interference between many microrays, saturates at unity (Fig. 9). As μ or range increases, however, correlation times or lengths will continually decrease.

There are two distinctive ways in which saturation can be achieved, depending on the relationships of the Fresnel zone, the correlation length (L_V), the strength parameter Φ , and the power-law spectral index. Qualitatively, the effect can be understood by discussing a case in which $R_F \ll L_V$, and another in which $R_F \gg L_V$. In the latter (Fig. 10(a)), the microrays are uncorrelated to first approximation and the received Ψ is a sum of many uncorrelated complex phasors. The result is a two-dimensional random walk called full saturation; the intensity PDF will be exponential (Rayleigh amplitude distribution). If $R_F \ll L_V$, then the larger-scale medium fluctuations change the

phase of all microrays together, so that the received wavefunction phase is directly correlated with the large-scale medium fluctuations. However, since Ψ is still the sum of many microrays, the small-scale medium fluctuations cause the amplitude to have a Rayleigh distribution to first approximation (corrections will be discussed later). Fig. 10(b) illustrates this behavior. This region is called partial saturation because of the still active relationship of phase to large-scale and amplitude to small-scale fluctuations that applies to the unsaturated region.

The actual behavior of the phase in partial saturation depends upon the relationships within the medium between large and small-scale fluctuations. For example, a wind advecting a frozen medium moves fluctuations by a point in a time proportional to the fluctuation wavelength. Such behavior yields a phasor behavior that is dominated by the small-scale-induced random walk, as in full saturation; the phase drift induced by the large scales is hardly noticeable. The temporal behavior of internal waves, however, is quite different, since it is controlled by a wave-dispersion

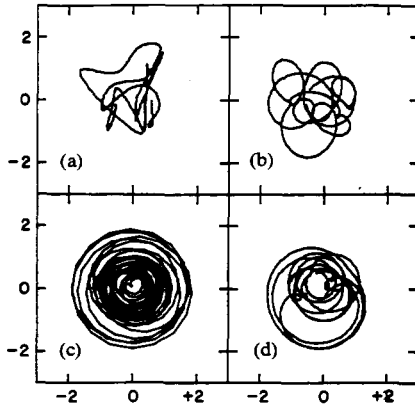


Fig. 11. Numerical simulations of saturated phasors in ocean acoustics. The time duration of the trace is approximately twenty times the intensity decorrelation time. (a) Full saturation; a two-dimensional random walk. (b) Partial saturation with the phase rate caused by the large-scale size fluctuations (ν) being 1.4 times the intensity decorrelation rate (ν'). (c) Partial saturation with $\nu/\nu' = 3.3$. (d) Partial saturation with $\nu/\nu' = 10$.

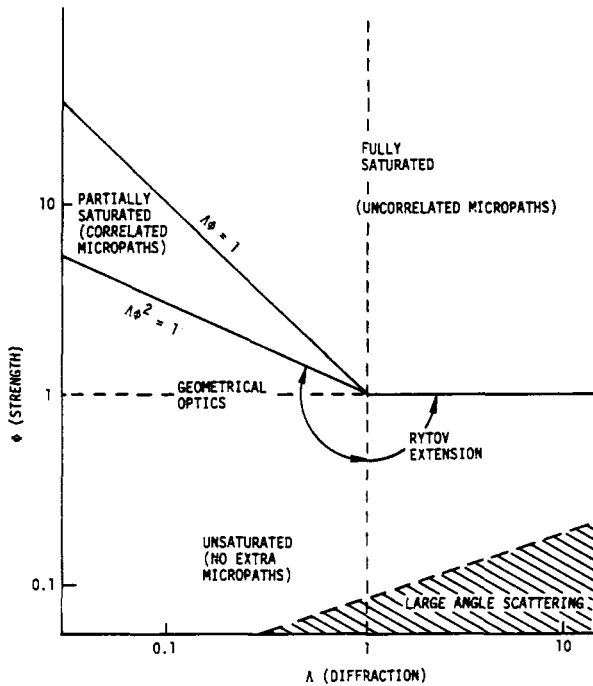


Fig. 12. Regions in Λ - Φ space.

relation in which the larger scale waves move faster. Thus the phase moves more rapidly than the amplitude in partially saturated ocean acoustics (Fig. 11).

The determination of the boundaries between the three important regions is an exercise in understanding the relation between spectral index and strength of fluctuations [24], [30]. For ocean internal waves, the result is shown in the Λ - Φ diagram (Fig. 12). The only region not covered in the above discussion is the Rytov section of the unsaturated region that is dominated by diffraction ($\Lambda > 1$). No ocean-acoustics experiments are likely to make significant measurements in that region, because it would require a Fresnel-zone diameter of order 1 km. In fact, ocean acoustics experiments are for the most part clustered within or close to the partially saturated region (Fig. 13).

The path-integral method has infused the above qualitative discussion with strong physical insight. Quantitatively rigorous results for various properties of the received wavefunction are based on the use of (40). The ensemble average of path integrals

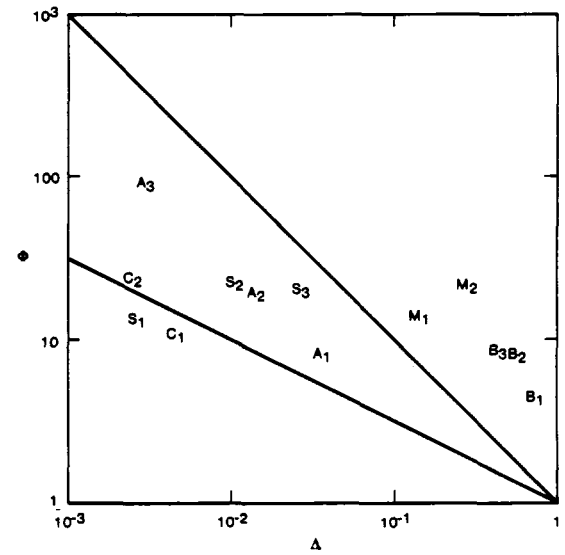


Fig. 13. Ocean-acoustics experiments placed on the Λ - Φ diagram. The 35-km AFAR experiment [64], [65] is A , with $A_1 = 410$ Hz, $A_2 = 1010$ Hz, and $A_3 = 4671$ Hz. The 23-km San Diego experiment [33] is S , with S_1 = upper and lower, S_2 = early upper I, and S_3 = early upper II. The 18-km Cobb experiment [69] is C , with $C_1 = 4$ kHz and $C_2 = 8$ kHz. The 900-km Bermuda experiment [32] is B , with B_1 = early, B_2 = middle, and B_3 = late rays. The 406-Hz MIMI experiment [24] is M , with $M_1 = 550$ km and $M_2 = 1250$ km.

will be computed, which requires the following formula:

$$\langle \exp \{ i\alpha \} \rangle = \exp \left\{ -\frac{1}{2} \langle \alpha^2 \rangle \right\}. \quad (42)$$

In general α will be some type of $q/\mu ds$ or the difference between such integrals. Thus the above formula, which is true for Gaussian random variables, will be rigorously true if μ is a Gaussian random variable (GRV) at every point. However, (42) is actually valid even if μ is not a GRV, provided that [31]

$$qL_V \langle \mu^2 \rangle^{1/2} \ll 1. \quad (43)$$

B. Moments of the Received Wavefunction

The First Moment: The first moment may be obtained from (40) and (42)

$$\begin{aligned} \langle \Psi \rangle &= \left\langle N \int d(\text{path}) \exp \left[iqS_0(\text{path}) - iq \int_{\text{path}} \mu dx \right] \right\rangle \\ &= N \int d(\text{path}) \exp \left[iqS_0(\text{path}) - \frac{1}{2} \left\langle \left(q \int_{\text{path}} \mu dx \right)^2 \right\rangle \right]. \end{aligned} \quad (44)$$

We may replace $\langle (q \int \mu dx)^2 \rangle$ by Φ^2 for all paths. Then the definition of N implies that

$$\langle \Psi \rangle = \exp \left(-\frac{1}{2} \Phi^2 \right). \quad (45)$$

The expression $\langle \Psi \rangle$ is sometimes called the coherent part of the wavefunction. Since $\Phi^2 \geq 1$ in the fully or partially saturated regime, $\langle \Psi \rangle$ is exponentially small and therefore not particularly interesting. The same is true for $\langle \Psi \Psi^* \rangle$ and its complex conjugate $\langle \Psi^* \Psi \rangle$. The validity of (44) depends only on replacing $\langle (q \int \mu ds)^2 \rangle$ along any important path by the same expression evaluated along the ray. We will discuss this type of validity at the end of this section.

The Second Moment: A more interesting quantity is

$\langle \Psi^*(2)\Psi(1) \rangle$ sometimes called the mutual coherence function, where 2 and 1 represent two different end points for paths 2 and 1. Multiplying the path integral for $\Psi(1)$ by the complex conjugate of the path integral for $\Psi(2)$ leads to a double-path integral, one of which connects the source to the observation point 1 and the other connects the source to 2. The result is

$$\begin{aligned} \langle \Psi^*(2)\Psi(1) \rangle &= \left\langle |N|^2 \int d^2(\text{path}) \exp \left[iqS_0(1) - iqS_0(2) \right. \right. \\ &\quad \left. \left. - iq \int_{\text{path 1}} \mu dx + iq \int_{\text{path 2}} \mu dx \right] \right\rangle \\ &= |N|^2 \int d^2(\text{path}) \exp \left[iqS_0(1) - iqS_0(2) - \frac{1}{2} V_{12} \right] \end{aligned} \quad (46)$$

where

$$V_{12} = q^2 \left\langle \left(\int_{\text{path 1}} \mu dx - \int_{\text{path 2}} \mu dx \right)^2 \right\rangle. \quad (47)$$

Now change the path variables to

$$u(x) \equiv z_1(x) - z_2(x)$$

and

$$w(x) \equiv \frac{1}{2} [z_1(x) + z_2(x)] \quad (48)$$

where $z_1(0) = z_2(0)$; $z_1(R) = (1)$; and $z_2(R) = (2)$. The path integral becomes

$$\begin{aligned} \langle \Psi^*(2)\Psi(1) \rangle &= |N|^2 \int d^2(\text{path}) \exp \left[iq \int_0^R dx \left[\partial_x u(x) \partial_x w(x) \right. \right. \\ &\quad \left. \left. + u(x) \partial_x U_0(x) w(x) \partial_x U_0(x) \right] - \frac{1}{2} V_{12} \right]. \end{aligned} \quad (49)$$

The endpoint conditions are

$$\begin{aligned} u(0) &= 0 \\ u(R) &= (2) - (1) \\ w(0) &= z_1(0) \\ w(R) &= \frac{1}{2} [(2) + (1)]. \end{aligned} \quad (50)$$

And it is understood that $U_0(x)$ is evaluated along the ray from $w(0)$ to $w(R)$. Now the crucial observation is that V_{12} is a function mainly of u and not of w . If V_{12} is not a function of w for any significant combinations of the two paths, in analogy with the formula

$$\int_{-\infty}^{\infty} da e^{ia\beta} = 2\pi\delta(\beta) \quad (51)$$

we expect the integral over paths $w(x)$ to yield delta functions. This has been rigorously verified [31]. When the relation

$$\begin{aligned} \exp \left[iq \int_0^R \partial_x u(x) \partial_x w(x) dx \right] \\ = \exp \left[-iq \int_0^R w(x) \partial_{xx} u(x) dx \right] \end{aligned} \quad (52)$$

is used, we see that u must satisfy

$$\partial_{xx} u(x) + U_0'' u(x) = 0. \quad (53)$$

This is just the equation that results if $u(x)$ is the separation of two nearby rays. The fact that no stationary-phase approximation has been invoked should be emphasized. But V_{12} for path 1 and 2 being nearby rays yield the phase-structure function from (34)

$$V_{12} = D(1, 2). \quad (54)$$

We then have a product of $\exp[-\frac{1}{2}D(1, 2)]$ and the path integral for the unperturbed intensity which is again normalized to one. Thus the result is

$$\langle \Psi^*(2)\Psi(1) \rangle = \exp \left[-\frac{1}{2} D(1, 2) \right]. \quad (55)$$

The result (55) has been obtained previously in many different ways [5], [54], [55]; in our view no other derivation has demonstrated the generality of (55), as the only approximations here [31] have been the parabolic approximation and that $V_{12} \neq f(w)$. The result is valid in the presence of inhomogeneity, anisotropy, a deterministic wave-speed profile, and regardless of whether the scattering is unsaturated or not, provided the approximation is valid. This will be discussed at the end of this section.

The Fourth Moment: Beyond $\langle \Psi^*(2)\Psi(1) \rangle$ the first nontrivial object is $\langle \Psi^*(4)\Psi(3)\Psi^*(2)\Psi(1) \rangle$, which has within it $\langle I^2 \rangle$ and $\langle I(2)I(1) \rangle$. It is given by the quadruple path integral over four paths $z_1(x), \dots, z_4(x)$

$$\langle I^2 \rangle = \frac{1}{(2q)^4} \int d^4(\text{path}) \exp \left[-iq \sum_{j=1}^4 (-1)^j S_0(j) - \frac{1}{2} M \right] \quad (56)$$

where the normalization factor is included and

$$M = q^2 \left\langle \left(\sum_{j=1}^4 (-1)^j \int_{\text{path } j} \mu dx \right)^2 \right\rangle. \quad (57)$$

We search for regions of path space that contribute significantly to (56). In the saturated regime, where Φ is large, $\exp(-\frac{1}{2}M)$ is extremely small except where paths are pairwise close. There are two regions of path space where M is of order one or smaller. They are

$$\begin{aligned} (a) &\equiv \left(|z_1(x) - z_2(x)| < \frac{L_V}{\Phi} \cap |z_3(x) - z_4(x)| < \frac{L_V}{\Phi} \right) \\ (b) &\equiv \left(|z_1(x) - z_4(x)| < \frac{L_V}{\Phi} \cap |z_3(x) - z_2(x)| < \frac{L_V}{\Phi} \right). \end{aligned} \quad (58)$$

In each of these regions there are two pairs of paths (12 and 34 in region a ; 14 and 23 in region b). The components of each pair are within a small fraction of a correlation length of each other (L_V/Φ). The crucial question is: how close is one pair from the other? We will answer this question only for the saturated regions, since intensity correlations in the unsaturated region are not particularly interesting compared with those of log intensity (see Section III-D). As a result we consider endpoint separations that are small compared with a Fresnel zone in what follows.

Full saturation: In the next paragraph we will prove that the average separation between pairs is large enough so that they are close to being uncorrelated even when the endpoints coincide. This is important because if they are completely uncorrelated, (57) can then be rewritten as

$$\begin{aligned} M \approx q^2 \left\langle \left(\int_{\text{path 1}} \mu dx - \int_{\text{path 2}} \mu dx \right)^2 \right. \\ \left. + \left(\int_{\text{path 3}} \mu dx - \int_{\text{path 4}} \mu dx \right)^2 \right\rangle \end{aligned} \quad (59)$$

where the cross terms have dropped out due to the decorrelation. Using (47)

$$M \approx V_{12} + V_{34}. \quad (60)$$

Similar results hold for region *b*. Thus in each of the two important regions in path space, the quadruple path integral factors into the product of two double path integrals, each of which is precisely the integral encountered earlier in the calculation of $\langle \Psi^* \Psi \rangle$. The result is that

$$\begin{aligned} \langle \Psi^*(4) \Psi(3) \Psi^*(2) \Psi(1) \rangle &\approx \langle \Psi^*(4) \Psi(3) \rangle \langle \Psi^*(2) \Psi(1) \rangle \\ &+ \langle \Psi^*(2) \Psi(3) \rangle \langle \Psi^*(4) \Psi(1) \rangle. \end{aligned} \quad (61)$$

For the case in which the end points of paths 2 and 3 coincide and paths 4 and 1 coincide

$$\langle I(2) I(1) \rangle = 1 + \exp \{ -D(2, 1) \} \quad (62)$$

where the two terms come from the regions *a* and *b*. Equation (62) is not exact because the pairs are not completely decorrelated. It is the explicit construction of the correlation that allows us to calculate the corrections to (61).

The proof of approximate pair decorrelation depends on showing that the average separation between pairs is much larger than L_V . The path integral (56) requires the addition of all path configurations for which the argument of the exponential is small. The value of M is kept small by considering only configurations with two pairs of close paths. The important path pairs are those for which the oscillating phase factor is also kept small, e.g.,

$$|qS_0(1) - qS_0(2)| \leq 1. \quad (63)$$

It can be shown [56] that each pair is separated from the equilibrium ray by a distance that is $\Lambda\Phi$ times the medium correlation length in the fully saturated region. In the fully saturated regime, $\Lambda\Phi \gg 1$ and over most of the integration volume the pairs of paths are separated by more than L_V and are therefore uncorrelated.

Partial saturation: In the partially saturated region, all the microrays are correlated by the large-scale fluctuations, but the small-scale fluctuations yield the two-dimensional random-walk behavior. If points 2 and 1 are separated in space, the behavior of M is dominated by the small-scale fluctuations, and the above arguments for full saturation go through to give (62). The temporal behavior of internal waves forces a quite different result for time separation [24]. The whole discussion of the difference between spatial and temporal behavior in the partially saturated region will not be reproduced here. However, a qualitative statement can be made; $\langle \Psi^*(\Delta z) \Psi(0) \rangle$ is controlled by the derivative of $D(\Delta z)$ with respect to Δz . Since the spectrum is like k_V^{-2} , the derivative spectrum is white, and therefore dominated by the small scales. On the other hand, $\langle \Psi^*(\Delta t) \Psi(0) \rangle$ is controlled by the derivative of $D(\Delta t)$ with respect to Δt . The internal-wave spectrum factorizes, so that $D'(\Delta t)$ is like k_V^{-2} and dominated by large scales. The result is that in partial saturation, (62) is replaced by

$$\langle I(\Delta t) I(0) \rangle = 1 + K(\Delta t) \quad (64)$$

where the path integral expression $K(\Delta t)$ can be calculated by integrating an ordinary differential equation with matrix coefficients (Appendix I). Effectively $K(\Delta t)$ is like $\exp \{ -D_s(\Delta t) \}$ where $D_s(\Delta t)$ is $D(\Delta t)$ with the large-scale fluctuation removed.

Both (62) and (64) lead to the same result for the simplest fourth moment

$$\langle I^2 \rangle \approx 2 \langle I \rangle^2 \quad (65)$$

that is, the variance of intensity (also called the scintillation index) is unity. (It is understood that $\langle I \rangle = 1$ by normalization

in most of the above derivations.) The reason for the validity of (65) in the partially saturated region may be traced to the fact that there are many microrays, and though they are separated by less than L_V , they are essentially decorrelated by the smaller scales. Of course, the intensity spectrum as a function of spatial or temporal frequencies is obtained from the Fourier transform of (62) or (64).

Higher Moments: The calculation of the n th moment of intensity $\langle I^n \rangle$ proceeds in a similar way. There are now $n!$ important regions of path space corresponding to the $n!$ ways of pairing a path from a Ψ with another one from a Ψ^* . In each of these regions the " $2n$ -tuple" path integral can be approximated by the product of n double-path integrals with the result that

$$\langle I^n \rangle \approx n! \langle I \rangle^n. \quad (66)$$

We have thus derived Rayleigh statistics (66), and have indicated that the inadequacy of (66) will depend on the correlation between pairs of microrays. Corrections to (66) will be described in Section VII. This approximation gets worse as n increases. When Φ is large, the average of any path integral will be exponentially small unless there is a region of path space where each path associated with a Ψ is close to a path associated with a Ψ^* . Such a region does not exist for $\langle \Psi \rangle$ or $\langle \Psi \Psi \rangle$, and we have already seen that they are exponentially small. More generally, any moment with an unequal number of Ψ 's will be vanishingly small.

C. Corrections to Rayleigh Statistics

We have said that the Rayleigh statistics result (66) requires corrections due to the correlations between microrays. The first correction has been worked out in detail [56], and the result is

$$\langle I^n \rangle \approx n! \langle I \rangle^n \left[1 + \frac{1}{2} n(n-1) \gamma \right] \quad (67)$$

where γ , the microray focussing parameter, is given by

$$\begin{aligned} \gamma &= q^2 \int_0^R dx \langle \mu^2(z_{\text{ray}}) \rangle L_P(\vartheta, z_{\text{ray}}) \int dk_V 2\tilde{f}(k_V; \vartheta, z_{\text{ray}}) \\ &\cdot \left[1 - \cos \left(\frac{k_V^2}{q} g(x, x) \right) \right] \exp \left[-q^2 \int_0^R \langle \mu^2(z'_{\text{ray}}) \rangle \right. \\ &\cdot L_P(\vartheta', z'_{\text{ray}}) f(\Delta z'; \vartheta, z'_{\text{ray}}) dx' \left. \right] \end{aligned} \quad (68)$$

$$\Delta z' = \frac{k'_V}{q} g(x', x'). \quad (69)$$

This correction will break down at large n , in fact for $n^2 \geq 2/\gamma$. The result of this correction is a tail on the probability density function for intensity. The particular distribution that corresponds to our case is not known, although the K function [57], [58] does have the same moments to first order.

Evaluation of γ from internal-wave fluctuation is accomplished by replacing

$$\int dk_V \tilde{f}(k_V; \vartheta, z_{\text{ray}}) \rightarrow \sum_j \frac{M_j}{j(j^2 - j_*^2)} \quad (70)$$

$$k_V \rightarrow \frac{jn(z)\pi}{n_0 B}. \quad (71)$$

Approximations for γ can be evaluated when there is no sound channel ($U_0'' = 0$) and it can be shown that the summation is dominated by low j in the fully saturated region, and by $j \gg j_*$ in the partially saturated region. If the weighting along the ray is

relatively uniform it is found that

$$\gamma \approx \frac{3}{2 \ln \Phi} \quad \text{partial saturation} \quad (72)$$

$$\gamma \approx \frac{0.83}{[\ln \Phi]^{3/2}} \frac{1}{\Lambda \Phi} \quad \text{full saturation.} \quad (73)$$

However, these approximations are extremely sensitive to non-zero U_0'' .

D. Phase and Log-Intensity Fluctuations

In the unsaturated region, it has long been known that the phase and log intensity are GRV's. The derivation of these results are based in one way or another on perturbation expansions. The result of such efforts are expressions for the variances of phase and log intensity. For the phase variance we have

$$\langle \varphi^2 \rangle = q^2 \int_0^R dx \langle \mu^2(z_{\text{ray}}) \rangle L_P(\varphi, z_{\text{ray}}) \cdot \int \left\{ \frac{1}{2} \tilde{f}(k_\nu; \vartheta, z) [1 + \cos(k_\nu^2 g(x, x)/q)] \right\} dk_\nu \quad (74)$$

where \tilde{f} is the Fourier transform of $f(\Delta z; \vartheta, z)$. In the geometrical optics part of the unsaturated region, the argument of the cosine is effectively zero and the integral over k_ν is unity, so that $\langle \varphi^2 \rangle = \Phi^2$. For log intensity we have

$$\langle (\ln I)^2 \rangle - \langle \ln I \rangle^2 = q^2 \int_0^R dx \langle \mu^2(z_{\text{ray}}) \rangle L_P(\vartheta, z_{\text{ray}}) \cdot \int \left\{ 2 \tilde{f}(k_\nu; \vartheta, z) [1 - \cos(k_\nu^2 g(x, x)/q)] \right\} dk_\nu. \quad (75)$$

In geometrical optics we then have the problem of integrating over the spectrum of a quantity very near zero. One cannot expand the cosine because the spectrum is not falling fast enough. A careful evaluation of the k_ν integral for small $g(x, x)/q$ gives

$$\int \left\{ 2 \tilde{f}(k_\nu; \vartheta, z) [1 - \cos(k_\nu^2 g(x, x)/q)] \right\} dk_\nu = \frac{\pi}{2} g(x, x)/q L_\nu^2 \quad (76)$$

and hence, from (37),

$$\langle (\ln I)^2 \rangle - \langle \ln I \rangle^2 \approx C \Lambda \Phi^2 \quad (77)$$

in the geometrical optics region. The constant C was taken as unity in [24] but here is more accurately $\pi/2$.

The frequency spectrum of phase and amplitude in this region is identical to the frequency spectrum of internal waves (30) because of the factorized nature of the spectrum, to first approximation (see Section VIII).

Full Saturation: The complex phasor Ψ does a two-dimensional random walk in full saturation, and the coherence function is given by (55), determining all statistics to first approximation. Because of the exponential character of (55), only the small-separation behavior of $D(1, 2)$ is relevant. For example, we may approximate

$$D(\Delta t) \approx \nu^2 (\Delta t)^2 \quad (78)$$

where ν is calculable from [52]

$$\nu^2 = q^2 \int_0^R dx \langle \mu^2(z_{\text{ray}}) \rangle L_P(\vartheta, z) \int \left\{ \tilde{f}(\omega, \vartheta, z) \omega^2 \right\} d\omega. \quad (79)$$

In that case, the phase and log-intensity spectra have been numerically approximated by [24]

$$S_{\nu, \varphi}(\omega) = \frac{\nu^2}{\omega^2 (\omega^2 + 1.27 \nu^2)^{1/2}} \quad (80)$$

$$S_{\nu, \ln I}(\omega) = \frac{4 \nu^2}{(\omega^2 + 2.43 \nu^2)^{3/2}}. \quad (81)$$

Partial Saturation: As a function of Δt , the phasor in the partially saturated region may be considered as the product of two functions (Fig. 10)

$$\Psi(\Delta t) = \exp[i\varphi_0(\Delta t)] \chi(\Delta t) \quad (82)$$

where $\chi(\Delta t)$ represents the interfering microrays that come from the small-scale medium fluctuations and $\varphi_0(\Delta t)$ is an overall phase from the large-scale fluctuations that correlate all the microrays. The spectrum of φ_0 is the same as the spectrum of φ in geometrical optics, while the spectrum of the phase of χ is the same as that of a fully saturated phasor with a different value of ν . If we approximate $K(\Delta t)$ from (64) by

$$K(\Delta t) \approx \exp\{-\nu'^2 \Delta t^2\} \quad (83)$$

then the spectrum of φ is the sum of two contributions

$$S_\varphi(\omega) = \frac{d\Phi^2}{d\omega} + S_{\nu', \varphi}(\omega) \quad (84)$$

where the first is the φ_0 contribution and the second is the χ contribution.

The log-intensity spectrum comes only from the χ contribution and hence should be given by (81) with ν replaced by ν' . Corrections to the assumption that χ and φ_0 are independent have not been worked out as yet.

E. Correlations in Frequency and Pulse Propagation

Pulse propagation is an area of great interest in wave transmission. Previous sections have dealt with monochromatic sources, but now we consider two different frequencies σ_1 and σ_2 . For any given microray one can easily show that

$$\langle \Psi^*(\sigma_1) \Psi(\sigma_2) \rangle = \exp\left[-\frac{1}{2} \left(\frac{\Delta\sigma}{\sigma}\right)^2 \Phi^2\right] \quad (85)$$

where $\sigma = (\sigma_1 + \sigma_2)/2$ and $\Delta\sigma = \sigma_2 - \sigma_1$. However, the total wavefunction in the saturated region is the sum of many microrays. We may write the corrected result in the form [24]

$$\langle \Psi^*(\sigma_1) \Psi(\sigma_2) \rangle = \exp\left[-\frac{1}{2} \left(\frac{\Delta\sigma}{\sigma}\right)^2 \Phi^2\right] Q(\Delta\sigma) \quad (86)$$

where the Q factor is the result of microray interference. The Q factor dominates only in the fully saturated region. The expression for Q in terms of a path integral, and its evaluation in terms of an ordinary differential equation is given in Appendix II.

The physical meaning of (86) is the following: when the exponential factor is dominant, then a narrow pulse will be received as a narrow pulse which wanders in arrival time from one member of the ensemble to another. If the Q factor dominates then the received pulse is spread over a considerable Δt for each member of the ensemble. The time spread is typically of order $\sigma^{-1} \Lambda \Phi^2 \ln \Phi$, which is independent of σ to first approximation. Note that the pulse-spread shape is dependent upon the deterministic wave-speed profile (Section V-B).

F. Validity of the Approximations

The key to the validity of the path integral result for $\langle \Psi \rangle$ lies in the assumption that $\langle (q/\mu ds)^2 \rangle$ is independent of path. Other

validity requirements are similar; in particular the result for $\langle \Psi^*(2)\Psi(1) \rangle$ depends upon V_{12} being independent of the centroid of two nearby paths. The limitations on validity come from inhomogeneity and anisotropy.

Let us write $\langle (q/\mu ds)^2 \rangle$ in terms of the correlation function ρ (see (26)). We have

$$\left\langle \left(q \int \mu ds \right)^2 \right\rangle = q^2 \int_0^R ds \int_0^R ds' \rho(s, s') \quad (87)$$

where s and s' move along the same path (Fig. 14). Our requirement is that this total integral does not vary significantly with path. Then we are concerned that

$$\frac{\int ds \int_{\text{path 1}} ds' \rho(s, s') - \int ds \int_{\text{path 2}} ds' \rho(s, s')}{\int ds \int_{\text{path 1}} ds' \rho(s, s')} \ll 1. \quad (88)$$

The denominator is Φ^2/q^2 if the criterion is satisfied. Let us consider a ρ with correlation lengths L_H and L_V that are short compared with R . Then we may express

$$\int ds' \rho(s, s') \approx \langle \mu^2 \rangle L_E \quad (89)$$

where L_E is an effective integral correlation length along the path, and $\langle \mu^2 \rangle$ is given by (31).

Inhomogeneity: Suppose we consider two paths displaced vertically a distance Δ . We know that significant paths cannot be displaced by more than R_F from the equilibrium ray, so that Δ is at most R_F . Since the paths are not different in angle, the major difference between them will be due to $\langle \mu^2 \rangle$, we can take $L_E = L_P$, and (88) becomes

$$\Phi^{-2} q^2 \int dx R_F \partial_z [\langle \mu^2 \rangle L_P(\vartheta, z)] \ll 1. \quad (90)$$

This criterion can be numerically evaluated for any experiment, since all the quantities are known in terms of the internal-wave spectrum and the equilibrium ray (note (12)). Since R_F is a function of acoustic frequency, there will be a lower limit on acoustic frequency below which the criterion will fail, because R_F will have grown excessively large. Typical values of the frequency (f_i) giving unity for the left-hand side are 10–100 Hz, but each experiment must re-examine (90).

Anisotropy: Consider now two paths that cross each other but drift apart as a function of range, as if they had different angles with the horizontal (Fig. 14). Just as there is a limit on displacement between paths, so there is a limit on the vertical distance that significant paths may drift apart. We need only consider little path segments of length L_E , since the contributions to the integrals add incoherently beyond that. In a length L_E , a path may drift by a distance of order $(\lambda L_E)^{1/2}$ and no more, due to the limitations of diffraction. Note that the requirement for the validity of the parabolic approximation is then $(\lambda L_E)^{1/2} \ll L_E$. For the criterion (88) to be satisfied we require that $(\lambda L_E)^{1/2} \ll L_V$ in some average sense. Put into the form $L_E/qL_V^2 \ll 1$, this ratio resembles the quantity whose average is the definition of Λ given in (37), except that the global function $|g(x, x)|$ has been replaced by the local correlation length L_E . In other words, the anisotropy criterion may be stated as $\Lambda_{L_E} \ll 1$ where this is the Λ calculated for a range of L_E . Hence, in the absence of a rigorous derivation, the logical anisotropy criterion is

$$\frac{q^2 \int dx \langle \mu^2 \rangle L_P \{ L_E/qL_V^2 \}}{q^2 \int \langle \mu^2 \rangle L_P dx} \ll 1 \quad (91)$$

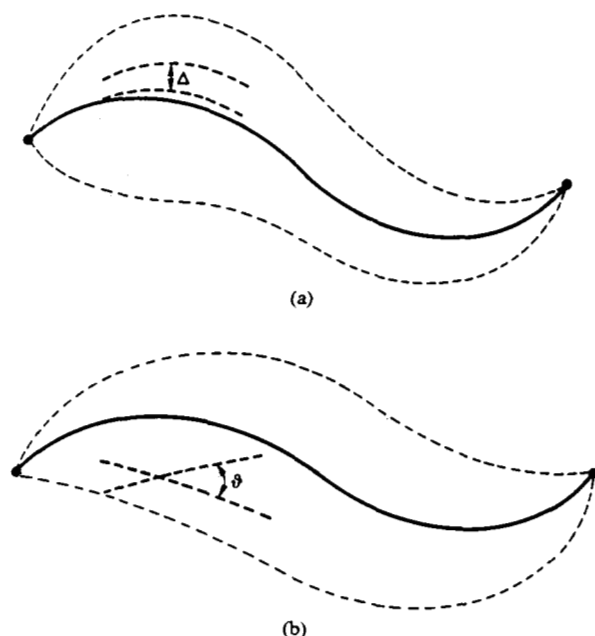


Fig. 14. Validity of the approximations used in evaluating path integrals. (a) Inhomogeneity will result in the integrals along two paths vertically separated by Δ having different values. (b) Anisotropy will give different integrals for two paths that lie within the Fresnel-zone tube around the ray; and which have different angles; only paths that have angles less than $(\lambda/L_P)^{1/2}$ contribute to the path integral in a significant way.

which can be expressed as

$$\Phi^{-2} q^2 \int_0^R dx \langle \mu^2 \rangle L_P \{ L_E/qL_V^2 \} \ll 1. \quad (92)$$

In most circumstances L_E can be taken to be L_P ; however, near the upper turning point of paths, the curvature of the path has an important effect. The curvature of the ray is U'_0 , so that a simple approximation to L_E would be $\{2L_V/U'_0\}^{1/2}$ if it is smaller than L_P . This correction to L_P makes a significant increase in the range of validity of the path-integral approximation for typical ocean rays. The integral (92) can be performed for any experimental configuration and the criterion thus evaluated will identify a lower frequency limit (f_A) of validity. Whether (90) or (92) will be the limiting effect will depend on the particular environmental conditions. A highly depth-dependent $\langle \mu^2 \rangle$, which can easily occur in the upper ocean, would make the inhomogeneity criterion more important. However, because the internal waves are inherently anisotropic, the anisotropy limit f_A will, in general, be higher than the inhomogeneity limit f_i . A limiting solution for the coherence function if $f \ll f_A$ has been determined [43], [44].

It is important to note that the validity criterion (88) would take a different form if the second moment were being considered instead of the first (and higher moments would require different modifications again). In particular, instead of using (33) along the path, one would use (35). The function $f(\Delta; \vartheta, z)$ is weakly dependent on z for internal waves; its dependence on ϑ is strong for $\Delta = \Delta t$ and weak for $\Delta = \Delta z$. The evaluation of the analog of (88) with f inserted after every ρ has not been systematically carried out as yet.

IV. THE MOMENT EQUATIONS

The technique of moment equations, which has enjoyed much development since the 1960's, begins with (39), traditionally ignoring the U_0 term. Since (40) is simply a solution of (39) all the same results should be derivable from the moment equation as

from the path integral. Indeed, the path integral results [24] for the second moment $\Gamma_2 = \langle \Psi^*(2)\Psi(1) \rangle$ have recently been derived with a U_0 term by moment equation techniques [41]. The moment equations depend on the parabolic approximation and on the Markov approximation (see Section IV-D).

The validity of the Markov approximation in an inhomogeneous anisotropic medium is difficult to ascertain. One reason is that the relation between the validity of the equation and the validity of a solution may be obscure; instances in which a given solution to an equation has a wider range of validity than the equation from which it is derived are all too familiar.

A. The Equations

To express the moment equations we need some notation. Let y_i and z_i be transverse coordinates from a horizontal line at y_0, z_0

$$\nabla_i^2 = \frac{\partial^2}{\partial y_i^2} + \frac{\partial^2}{\partial z_i^2} \quad (93)$$

$$A_0 = q^2 \int_{-\infty}^{\infty} \rho(x - x', 0, 0, 0) dx' \quad (94)$$

$$A_{ij} = q^2 \int_{-\infty}^{\infty} \rho(x_i - x', y_i - y_j, z_i - z_j, t_i - t_j) dx' \quad (95)$$

$$\Delta = y e_y + z e_z \quad \text{and} \quad t \quad (96)$$

$$\Gamma_1(x, \Delta) = \langle \Psi(x, y, z, t) \rangle \quad (97)$$

$$\Gamma_2(x, \Delta_1, \Delta_2) = \langle \Psi^*(x, y_1, z_1, t) \Psi(x, y_2, z_2, t_2) \rangle \quad (98)$$

$$\Gamma_4(x, \Delta_1, \Delta_2, \Delta_3, \Delta_4) = \langle \Psi_1 \Psi_2^* \Psi_3 \Psi_4^* \rangle. \quad (99)$$

Then the three usual moment equations are, from (39) with $U_0 = 0$, and the Markov approximation (see the following)

$$\partial_x \Gamma_1 = \left[-\frac{i}{2q} \nabla^2 - \frac{1}{2} A_0 \right] \Gamma_1 \quad (100)$$

$$\partial_x \Gamma_2 = \left[-\frac{i}{2q} (\nabla_1^2 - \nabla_2^2) - (A_0 - A_{12}) \right] \Gamma_2 \quad (101)$$

$$\partial_x \Gamma_4 = \left[-\frac{i}{2q} (\nabla_1^2 - \nabla_2^2 + \nabla_3^2 - \nabla_4^2) - (2A_0 + A_{13} + A_{24} - A_{12} - A_{23} - A_{14} - A_{34}) \right] \Gamma_4. \quad (102)$$

Note that

$$A_0 = q^2 \langle \mu^2(z_0) \rangle L_P(0; z_0) \quad (103)$$

$$A_{ij} = q^2 \langle \mu^2(z_0) \rangle L_P(0; z_0) f(\Delta_{ij}; 0, z_0). \quad (104)$$

Thus

$$\int_0^R A_0 dx = \Phi^2 \quad (105)$$

$$\int_0^R A_{ij} dx = \Phi^2 - D_P(i, j) \quad (106)$$

$$\int_0^R (A_0 - A_{12}) dx = \frac{1}{2} D_P(1, 2) \quad (107)$$

where we have used the symbol $D_P(i, j)$, since the separation Δ_{ij} is a constant as a function of x , while the previously defined $D(i, j)$ assumes a spatial separation starting at 0 at $x = 0$ and ending at Δ_{ij} at $x = R$.

B. Solutions for the First and Second Moments

The solutions for Γ_1 and Γ_2 are relatively simple if we assume that the Γ 's are independent of transverse coordinates. The ∇^2 then have no effect and we have

$$\Gamma_1 = \Gamma_{10} \exp \left\{ \frac{1}{2} \int_0^R A_0 dx \right\} = \Gamma_{10} \exp \left\{ -\frac{1}{2} \Phi^2 \right\} \quad (108)$$

$$\Gamma_2 = \Gamma_{20} \exp \left\{ -\int_0^R (A_0 - A_{12}) dx \right\} = \Gamma_{20} \exp \left\{ -\frac{1}{2} D_P(1, 2) \right\} \quad (109)$$

which are exactly the same as (45) and (55), except for the substitution of D_P for D . The above solution is associated with a plane wave rather than the point source of (55) because of the assumption of independence of transverse coordinate.

The moment-equation derivation of (109) has required the following set of additional assumptions beyond those used in the path integral derivation: straight-line ray in the absence of fluctuations, no inhomogeneity in the transverse direction, and plane-wave incidence. These limitations can of course be overcome if the limits imposed on inhomogeneity and anisotropy are imposed in the same way they were in deriving (55), but no solutions that are more general have been obtained [41]. Results for pulse propagation suffer from the same difficulties.

We can thus see that the whole concept of decomposition into plane waves becomes problematic in an inhomogeneous, anisotropic medium. The advantage of the path integral here is conceptual; when the frequency is high enough that the ray tube bounded by a Fresnel zone is quite restricted, it is advantageous to use a technique that automatically accounts for this fact, rather than treating it by a combination of plane waves that are infinite in extent.

C. Solutions for the Fourth Moment

Finding a direct solution to the fourth-moment equation has proven even more elusive than solving the lower order equations. One of the earliest successes [59], [60] was Shishov's determination of an asymptotic solution at large range, for which the method of "successive scatters" was developed. This method will not be discussed here since the same results are now more easily obtained by means of the path integral [9]. However, it is perhaps worthwhile to explain qualitatively the disadvantage of the method of multiple scatter (MMS), at least in ocean acoustics.

Qualitatively, MMS considers the coherent field (44) as being lost due to scattering [54]. The field may be considered as representing an incident flux of particles which are attenuated exponentially; the power in the exponent is the number of mean free paths for these particles, given by Φ^2 . The mean free path is quite long compared with a longitudinal correlation length, hence it is argued that each scatter is uncorrelated. The derivation continues from there. However, the argument is wrong, or at best misleading, in a medium whose transverse scale size is large compared with a Fresnel zone (Fig. 8(b)) and for a wave propagation with $\Phi \gg 1$. In that case, MMS involves a complicated sum of many possible orders of scatter. Yet the solution to that case is incredibly simple; it is a single ray from source to receiver whose phase has been advanced or retarded, with a phase variance of Φ^2 , and this solution is obtained in one line with the path integral.

With considerable work, the multiple scattering theory can be used by keeping careful track of the correlations between all the scatters. One major question that is unresolved as yet and that

perhaps could be treated by MMS is the problem of the second moment very near a caustic [40], [41].

Finally, a remark should be made on the low-frequency limit in which the anisotropy criterion (90) for the validity of the path integral results is violated. A theory for the opposite limit (i.e., $f \ll f_A$) has been developed for the second moment [43], [44] and some application to the low-frequency horizontal coherence function has been made. It is to be noted that the second-moment equation for the highly anisotropic case is different from (101).

D. The Markov Approximation

What assumptions have gone into the derivations of the moment equations (100)–(102) and how are they related to the conditions (90) and (92) for the validity of the path-integral solution? A brief discussion of the Markov approximation is useful. For example, consider the derivation of the equation for $\langle \Psi \rangle$. We begin by taking the expectation value of (39)

$$2iq\partial_x\langle\Psi\rangle = [-\nabla^2 + 2q^2U_0]\langle\Psi\rangle + 2q^2\langle\mu(x,t)\Psi(x)\rangle. \quad (110)$$

The last term provides the difficulty, since Ψ is correlated to the behavior of μ . If μ is a GRV, then [62], [63]

$$\langle\mu(x,t)\Psi(x)\rangle = N^{-1} \int dt' \int d^3x' \langle\mu(x,t)\mu(x',t')\rangle \left\langle \frac{\partial\Psi}{\partial\mu(x',t')} \right\rangle \quad (111)$$

where N is a normalization integral over x' and t' . In other words, the term in question involves the correlation function of μ and the functional derivative of Ψ with respect to μ over all space and time. The evaluation of this complex form can be done directly under the Markov assumption

$$\langle\mu(x,t)\mu(x',t')\rangle = \delta(x-x')A(y-y', z-z', t-t'). \quad (112)$$

The validity of this approximation has been explored [63] by a method of successive approximations in which the next term in a series is determined. The result is that (112) is justified if

$$(\lambda L_E)^{1/2} \ll L_V. \quad (113)$$

In other words, the requirement is a local version of (92). Hence the validity requirement for the Markov approximation and for the path integral evaluation are very closely related. Note that the approximation that A is not a function of $y+y'$ or $z+z'$ has been slipped into (112). If this were not assumed, then another limitation on the validity of Markov would be required, and it would be similar to (90).

The main difference between the criteria for Markov and for the path integral is that the path integral gives an explicit way to evaluate the global criteria with proper weighting while the Markov criteria are solely local. Thus the desire for a value of $\langle\Psi^*\Psi\rangle$ at some particular long range does not depend on Markov being valid everywhere, but only in a weighted sense along the equilibrium ray. In addition, the discussion above does not provide a framework for understanding the dependence of L_E on the background sound channel, which is known to be of considerable significance. (See discussion following (92).)

V. THE COHERENCE FUNCTION

Results for the coherence function, or in other words, the normalized second moment, derive from (55) in the case of time and space separations, or from (86) in the case of frequency

TABLE I
SUMMARY OF EXPERIMENTS

Reference	σ (Hz)	R (km)	Φ	$10^3\Lambda$	ν^{-1} (min)	ν'^{-1} (min)	$\Lambda\Phi$	$\Lambda\Phi^2$
COBB	4000	18	10	4.2	6.6	—	0.042	0.42
	8000	18	20	2.1	3.3	—	0.042	0.84
SD	2273	23						
	Lower		13	2.5	5.9	—	0.033	0.43
	Early Upper I		20	9.3	2.7	22	0.19	3.7
	Early Upper II		19	24.3	2.7	21	0.47	9.0
AFAR			13	2.3	2.6	—	0.031	0.42
	410	35	7.4	31	9.1	18	0.23	1.7
	1010	35	18	13	3.7	6.2	0.23	4.1
	4671	35	84	2.7	0.81	1.1	0.23	19
Bermuda	220	900						
	Early		4.1	640	10	10	2.6	11
	Middle		7.1	530	6.0	6.0	3.8	27
MIMI			7.2	390	5.8	5.8	2.8	20
	406	550	13	120	5.0	5.0	1.6	20
	406	1250	20	240	3.3	3.3	4.8	96

The experiments are roughly ordered from unsaturated ($\Lambda\Phi^2 < 1$) through partially saturated ($\Lambda\Phi < 1 < \Lambda\Phi^2$) to fully saturated ($1 < \Lambda\Phi$). The different rays in the SD and Bermuda experiments are labeled by their arrival sequence.

The decorrelation time of the complex phasor (ν^{-1}) is from (79). The intensity decorrelation time (ν'^{-1}) varies from ∞ in the unsaturated region down to being equal to ν^{-1} in the fully saturated region.

separations. The interest in these results is confined to the saturated regions where the second moment is a simpler quantity than the phase and amplitude separately. Three experiments have published relevant results. (See Fig. 13 and Table I.) The Miami-Michigan experiments [24] (MIMI) had a CW 406-Hz source on Eleuthera (Bahamas) and two receivers: one 550 km away (Midstation) and another 1250 km away near Bermuda. Data from a 26-day period were analyzed. The Azores Fixed Acoustic Range experiment [64], [65], [24] (AFAR) had frequencies of transmission varying between 410 and 4671 Hz with data obtained over a 35-km path. Pulses widths varied from 1.28 to 130 ms, and transmissions occurred every 10 s for 120 h. The San Diego (SD) experiment [33] used broad-band pulse transmissions centered at 2273 Hz transmitted for 72 h over a 23-km path off the coast of California. As can be seen from Fig. 13, two of these experiments (AFAR and SD) are in the partially saturated region, while the third (MIMI) is fully saturated.

A. Separations in Time

Fig. 15 shows the spectra of the real and imaginary parts of $\Psi(\Delta t)$ for the MIMI experiment. The approximation (78) may be used in (55) yielding a Gaussian correlation function in time, and hence a Gaussian frequency spectrum. The results are in excellent agreement with the predictions, including the predicted magnitude of ν obtained from (79) averaged over the large number of deterministic rays in this configuration.

Fig. 16 shows an estimate of $D(\Delta t)$ obtained in the AFAR experiment from $-2 \ln \langle \Psi^*(\Delta t)\Psi(0) \rangle$, compared with the internal-wave prediction using environmental measurements at the time of the experiment. The agreement is excellent for all three acoustic frequencies used. Thus the scaling of the exponent in (55) with q^2 is well verified, and the possibility of measuring $D(\Delta t)$ even in the saturated region [66] is supported.

B. Separations in Frequency

The distribution of arrival intensity averaged over many pulses, $\langle I(\tau) \rangle$, represents an average over frequency of the coherence

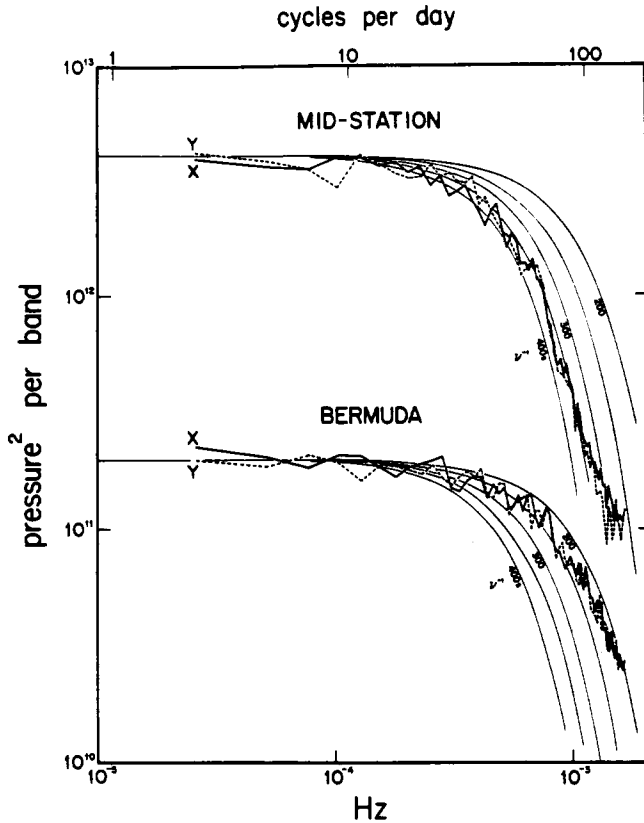


Fig. 15. Spectra of the real (X) and imaginary (Y) parts of the complex wavefunction $\Psi(t)$, per bandwidth 2.58×10^{-5} Hz. The computed curves use the approximation $D(t) \approx \nu^2 t^2$ so that the spectra have Gaussian shape.

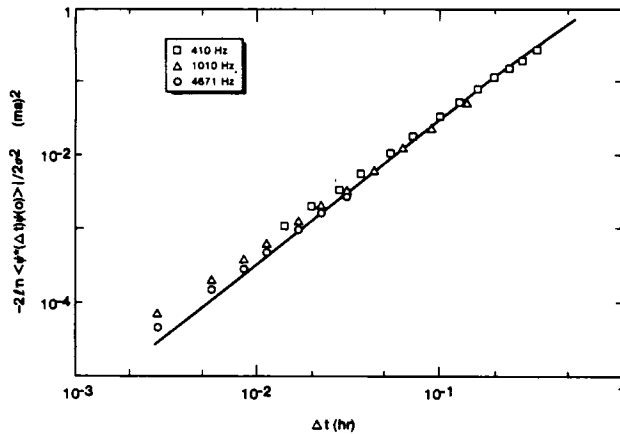


Fig. 16. Evaluation of the phase structure function in the partially saturated region by use of the coherence function. Statistical error bars are smaller than the symbols. The solid line is the prediction for $D(\Delta t)$ based on environmental measurements.

function of frequency. That is,

$$\langle I(\tau) \rangle = (2\pi)^{-1} \int_{-\infty}^{\infty} d\sigma \int_{-\infty}^{\infty} d(\Delta\sigma) X\left(\sigma + \frac{\Delta\sigma}{2}\right) X^*\left(\sigma - \frac{\Delta\sigma}{2}\right) \cdot \langle \Psi^*(\Delta\sigma) \Psi(0) \rangle \exp(i\Delta\sigma\tau) \quad (114)$$

where $X(\sigma)$ is the Fourier transform of the transmitted pulse. We normalize in such a way that

$$\int_{-\infty}^{\infty} I(\tau) d\tau = 1. \quad (115)$$

Fig. 17 shows the pulse from the AFAR experiment, compared with a calculation of $\langle I(\tau) \rangle$ using (86) with $Q(\Delta\sigma)$ and Φ calculated from environmental measurements. The prediction of

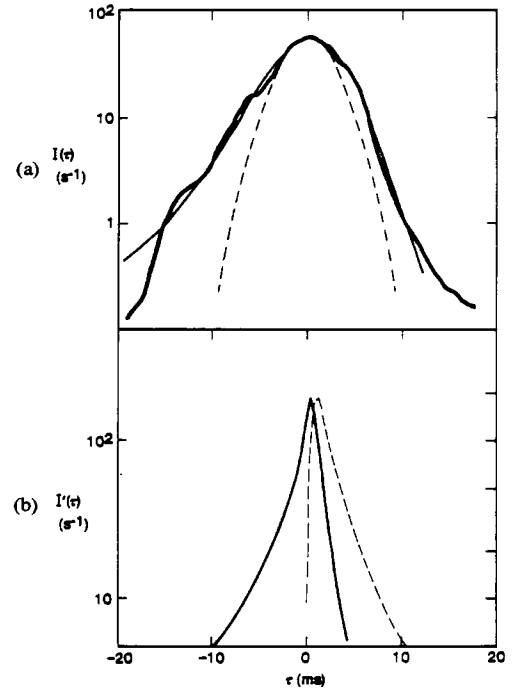


Fig. 17. Pulse extent in the AFAR experiment using transmission of a 1.28-ms pulse centered at 3200 Hz. (a) Average over many pulses $\langle I(\tau) \rangle$. The thin solid line is the prediction from (86), incorporating pulse wander (dashed line) and pulse spread. (b) If wander could be removed, the average individual pulse spread would be the solid curve. The sound channel has substantially altered the pulse shape from the no-sound-channel prediction (dashed line).

the exponential factor alone (dashed) gives reasonable pulse-width. The asymmetric shift toward early arrivals is a result of the action of the deterministic sound channel in its effect on $Q(\Delta\sigma)$; agreement between theory and experiment is striking.

Fig. 17(a) is not a prediction of the average appearance of a single pulse; a considerable part of the width of $\langle I(\tau) \rangle$ is due to the wander of the pulse with geophysical time. It is not possible to unambiguously remove this unknown wander in an experiment, but if one could, the average pulse would be considerably narrower. The prediction for the AFAR pulse in the absence of wander, obtained by removing the exponential factor in (86), is shown in Fig. 17(b). Also shown is the predicted pulse shape for no focussing by the sound channel, obtained by setting $U_0'' = 0$ in the calculation of $Q(\Delta\sigma)$. The no-sound-channel pulse shows the sharp rise and exponential fall that is expected from previous calculations (e.g., [54]), but the effect of the sound channel is strikingly significant; the pulse now has an approximately exponentially rising precursor, and a much sharper exponential fall after the pulse peak. Fig. 17(a) is the experimental confirmation of this effect.

A direct measurement of $\langle \Psi^*(\Delta\sigma) \Psi(0) \rangle$ can be extracted from the data since the transmitted pulse Fourier transform is known accurately. Fig. 18 shows this result compared with the prediction of (86). The effect of the sound channel is seen to be primarily on the phase of $Q(\Delta\sigma)$.

A similar result from the short-range SD experiment shows rough agreement with pulse extent (Fig. 19), but the amount of available data is meager. In this case also the pulse extent is dominated by the exponential factor; the $Q(\Delta\sigma)$ has a significant effect on $\langle I(\tau) \rangle$ only in the tail.

C. Separations in Vertical Position

Only the SD experiment has measured anything about correlations between receivers separated vertically, in their case by 30.5

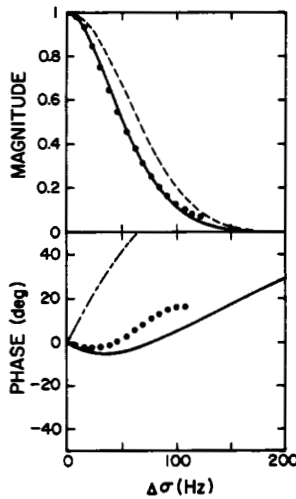


Fig. 18. The two-frequency mutual coherence function in the AFAR experiment [24] at 4671 Hz. The closed circles are experimental results of $\langle \Psi^*(\Delta\sigma)\Psi(0) \rangle$. The solid curves are calculations of the right-hand side of (86). The dash-dot curve is the phase result for no sound channel ($U_0'' = 0$). (The no-sound-channel magnitude is nearly coincident with the solid curve.) The dashed magnitude line is the wander effect only: that is, the right-hand side of (85).

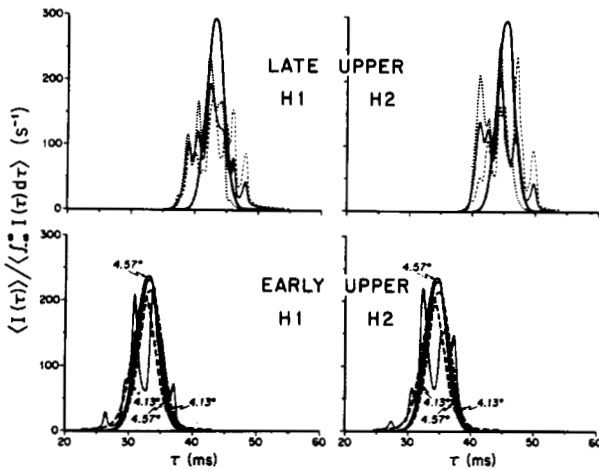


Fig. 19. Pulse extent, $\langle I(\tau) \rangle$, for the SD experiment [33].

m. This result of comparison between theory and experiment is shown in Fig. 20. The saturated ray (early upper) is in reasonably good agreement. The result for the other two rays, which are in the unsaturated region, will be discussed in the section on phase statistics (Section VIII-A).

D. Reciprocal Transmission

Although the effect of water velocity on effective sound speed is less than about 10 percent [24], it has been pointed out [67] that the statistical behavior of internal-wave currents could be measured by the technique of reciprocal transmission; that is, the measurement of differences between acoustic propagation in opposite directions. This is another coherence function, where the separation between rays may be not only Δt , but the direction of transmission. For example, define two rays between given points A and B at time t as t_+ and t_- for the ray traveling from A to B and the ray from B to A , respectively. Then, in general,

$$\langle \Psi_+^*(\Delta t)\Psi_-(0) \rangle = \exp\left\{-\frac{1}{2}D(\Delta t_+, 0_-)\right\} \quad (116)$$

so that a measurement of the mutual coherence function of time

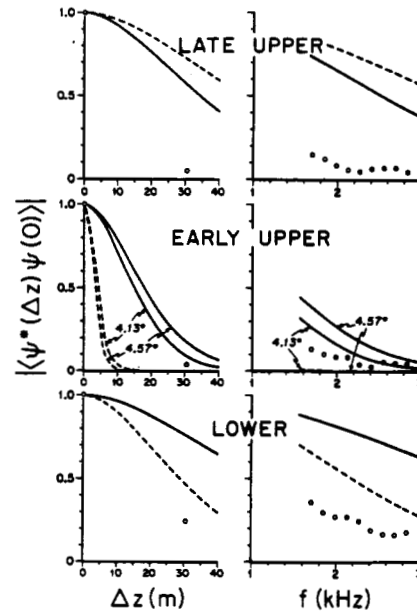


Fig. 20. The mutual coherence function for vertical separation from the SD experiment [33]. The heavy solid curves are predictions from (55), while the dashed curves are the same with $U_0''(z)$ smoothed with a running 70-m box average.

lag between these two rays can be used via (116) to measure the phase structure function $D(\Delta t_+, 0_-)$.

It has been pointed out that a combination of $D(\Delta t_+, 0_+)$, $D(\Delta t_-, 0_-)$, and $D(\Delta t_+, 0_-)$ can be used to measure an important statistical quantity related to horizontal currents: that is the vertical flux of horizontal momentum [66], [68]. The measurement involves the quadrature spectrum of $D(\Delta t, 0_-)$. The desired quantity is $\langle wu \rangle$ where u and w are horizontal and vertical velocity components. But $w = \partial_t \zeta$ where ζ is the vertical displacement of internal waves, which is taken as proportional to μ , the main fluctuation in sound speed due to internal waves. The actual measurement from reciprocal transmission is the spectrum of $\langle (\partial_t \mu)u \rangle$.

VI. INTENSITY COHERENCE: THE FOURTH MOMENT

Experimental results for the fourth moment are confined to correlations of intensity. The experiments that provide results in this section are AFAR, SD (see Section V), and an experiment at 220 Hz and 900-km range southwest of Bermuda [32]. The Bermuda experiment transmitted 64-ms pulses every 10 min continuously for several months; the environmental data allowed the calculation of Λ and Φ , and placed the experiment in the fully saturated region (Fig. 13).

A. Separations in Time

In the fully saturated region, the autocorrelation of intensity is given by (62)

$$r(\Delta t) = \langle I(\Delta t)I(0) \rangle - 1 = \exp[-D(\Delta t)]. \quad (117)$$

This equation does not include corrections to Rayleigh statistics; that is, it assumes that $\langle I^2(0) \rangle = 2$. The observed $\langle I^2(0) \rangle$ is generally greater than 2; to account for this fact the quantity $2\langle I(\Delta t)I(0) \rangle / \langle I^2(0) \rangle$ will be used as the experimental estimate of $\langle I(\Delta t)I(0) \rangle$ in (117).

Fig. 21 shows $r(\Delta t)$ for three rays in the Bermuda experiment. The observed distributions have roughly the correct initial falloff, but have longer tails than the internal-wave prediction. The tails are even more pronounced if frequency contributions beyond one

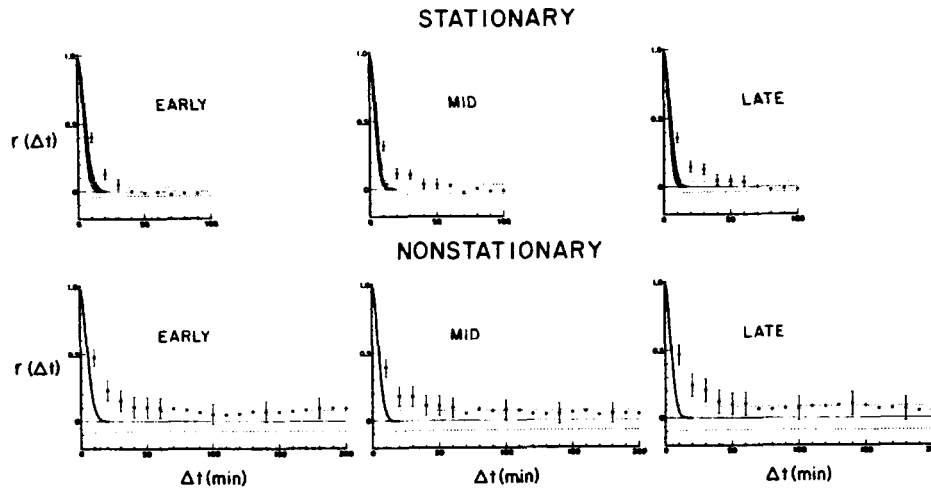


Fig. 21. Autocorrelation functions of intensity for the Bermuda experiment [32]. Theory for this fully saturated experiment is given by (117).

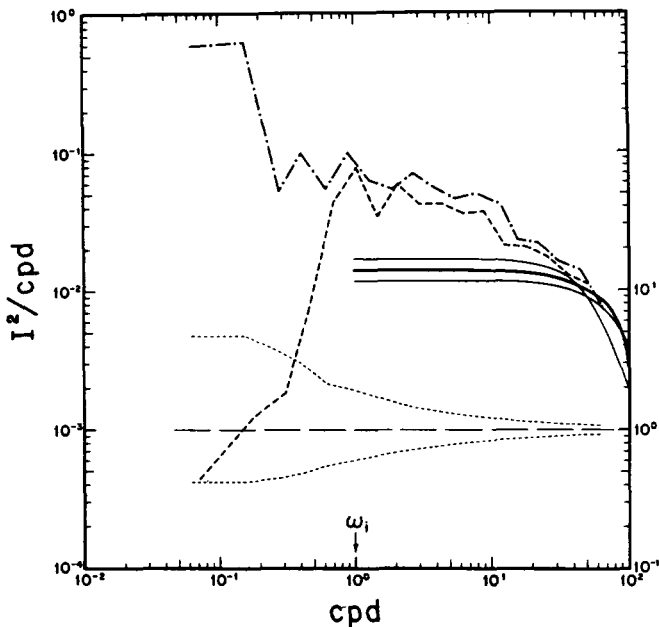


Fig. 22. Intensity spectrum for the Bermuda experiment [32]. Theory is Gaussian with ν given in Table I. The 95-percent confidence intervals (short dashed) are drawn relative to unity (right-hand scale).

cycle per day are retained. Fig. 22 shows the intensity spectrum (the Fourier transform of Fig. 21) with a prediction based on (78).

In the partially saturated regime, $r(\Delta t)$ is given by (64)

$$r(\Delta t) = K(\Delta t). \quad (118)$$

Fig. 23 shows $r(\Delta t)$ for the SD experiment. In this case, the observed distribution is narrower than the prediction. The prediction is substantially affected by small change in U_0'' , as illustrated by the dashed prediction from smoothing U_0'' by a 70-m box average.

Fig. 24 shows $r(\Delta t)$ for the AFAR experiment. Good agreement is obtained in this experiment, which has the highest level of both acoustic and environmental measurements. Note that the fully saturated prediction of $\exp[-D(\Delta t)]$ is quite inadequate. The data of AFAR are so good that the Fourier transform of Fig. 24 can be calculated: that is, the intensity spectrum. Fig. 25 shows the intensity spectrum compared with the Fourier transform of $K(\Delta t)$ as calculated from AFAR environmental parameters.

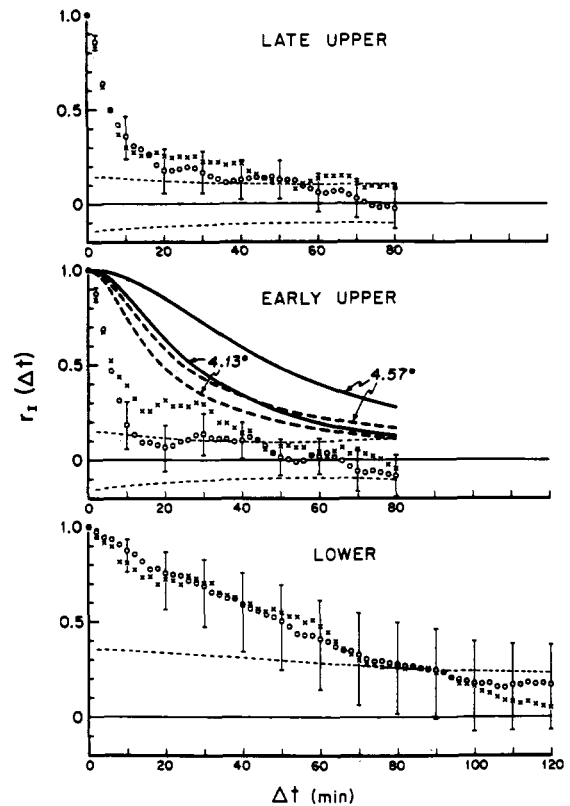


Fig. 23. Autocorrelation functions of intensity for the SD experiment [33]. The early upper ray is the only one in the saturated region (Table I). Theory (heavy solid line) is $K(\Delta t)$ calculated from environmental measurements, which predicted two indistinguishable rays with launch angles of 4.13° and 4.57° . The heavy dashed lines are $K(\Delta t)$ calculated with $U_0''(z)$ smoothed by a 70-m running box average.

ters. The agreement, including the scaling with acoustic frequency, is excellent, illustrating quantitative understanding of the partially saturated region.

B. Separations in Frequency

Intensity decorrelation with frequency in the saturated regions can be shown to follow approximately [24], [31]

$$r(\Delta\sigma) = |Q(\Delta\sigma)|^2. \quad (119)$$

Fig. 26 shows $r(\Delta\sigma)$ for the SD experiment. Again the sensitiv-

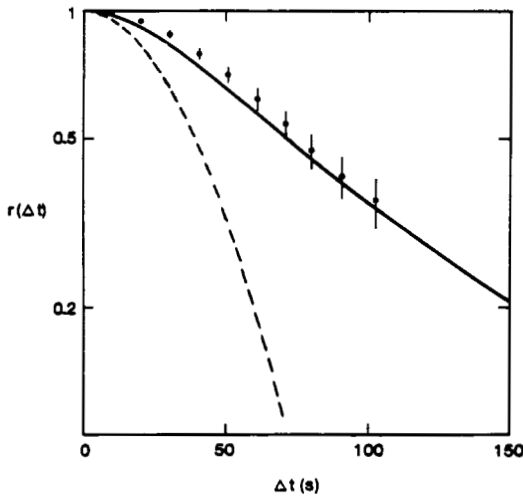


Fig. 24. Autocorrelation function of intensity for the AFAR experiment [24] at 4671 Hz. Theory is $K(\Delta t)$ calculated from environmental measurements. The dashed line is the result assuming full saturation: that is, $\exp[-D(\Delta t)]$.

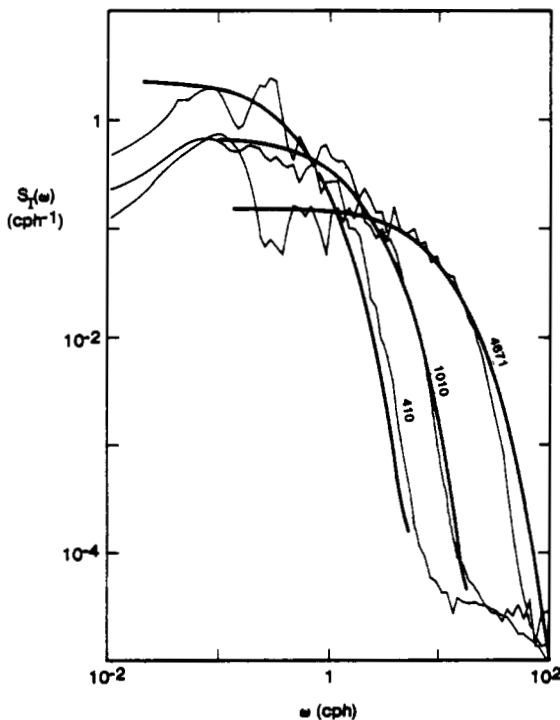


Fig. 25. Intensity spectra for the AFAR experiment [24]. Theory is the Fourier transform of $K(\Delta t)$.

ity to smoothing U_0'' is seen, but general agreement is reached. Fig. 27 shows $r(\Delta\sigma)$ for the Bermuda experiment. The results are in excellent agreement for all three rays. Fig. 28 shows $r(\Delta\sigma)$ for the AFAR experiment, where again agreement is reasonable.

C. Separation in Vertical Position

Only the SD experiment made measurements of vertically separated intensities. Fig. 29 shows $r(\Delta z)$ for that experiment. Since only one separation, 30.5 m, is available, the best that can be said is that the predictions are consistent with observations.

However, the Bermuda experiment did correlate the intensities of different deterministic rays, which are separated from each other by distances large compared to internal-wave vertical-correlation lengths over most of the range. The intensity fluctuations for these rays should therefore be uncorrelated for frequencies in

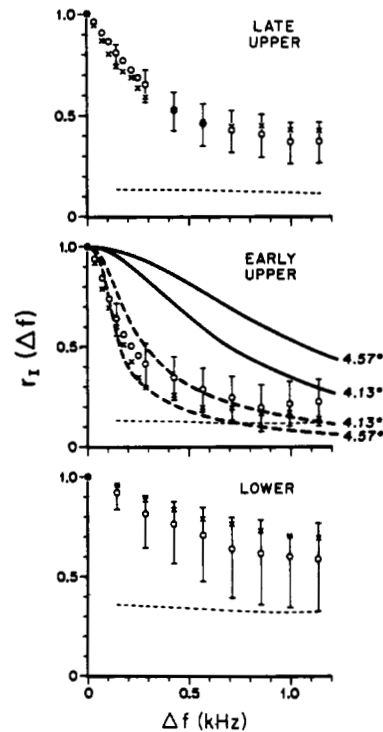


Fig. 26. Intensity correlation function of acoustic frequency for the San Diego experiment [33]. Calculations for the early upper path are from environmental measurements. The heavy dashed curves have 70-m smoothing on U_0'' .

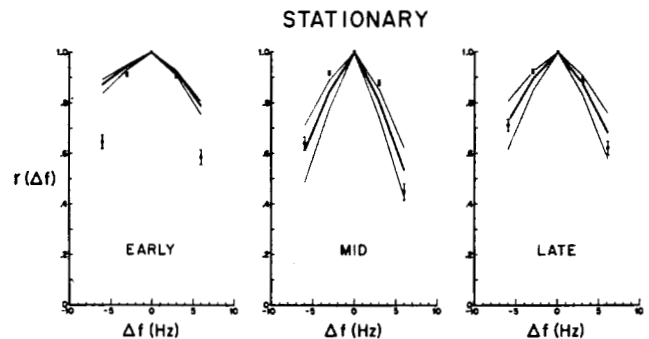


Fig. 27. Intensity correlation function of acoustic frequency for the Bermuda experiment [32]. The light solid curves show the effect of changing the internal-wave energy level by a factor of two.

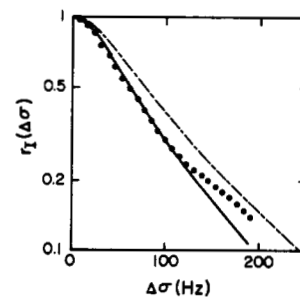


Fig. 28. Intensity correlation function of acoustic frequency for the AFAR experiment [24] at 4671 Hz. The dash-dot curve is the no-sound-channel result ($U_0'' = 0$).

the internal-wave band. There is no significant coherence (at the 95-percent confidence level) for either pair above 16 cycles/month. However there is considerable coherence near a few cycles/month (Fig. 30), which is presumably due to meso-scale activity.

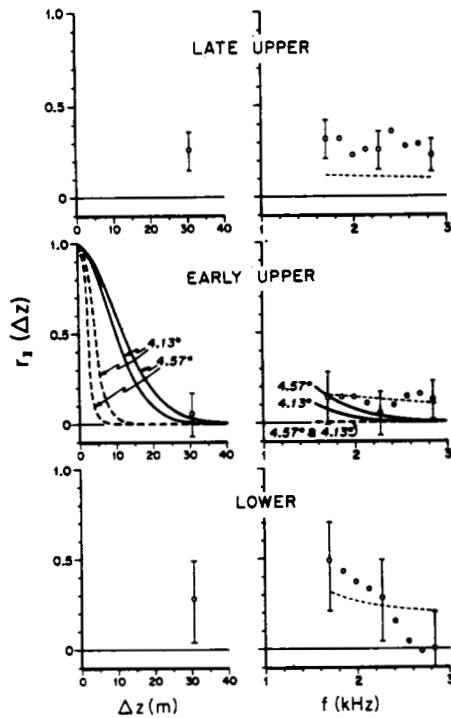


Fig. 29. Intensity correlation function of vertical separation for the SD experiment [33].

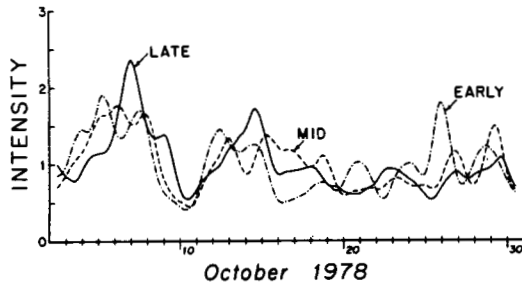


Fig. 30. Time series of intensity for three rays in the Bermuda experiment [32], low-pass filtered at 1 cycle/day, showing the correlation between rays separated vertically by kilometers.

VII. CORRECTIONS TO RAYLEIGH STATISTICS

The probability distribution of intensity has within it information on all the moments of intensity. The expectation for these moments is contained in (67)–(69). A detailed analysis of this aspect of the path-integral prediction is given in [56]. Table II shows the observed moments in three experiments, and demonstrates that the relation (67) is in close agreement with experiment when γ is taken as an unknown parameter. Table III gives results from numerical calculations of γ for these three experiments. The first row is from (72) and (73) and is seen not to be very accurate. Subsequent rows are from more accurate approximations to γ ; the top number is using $g(x, x)$ from a straight-line ray while the number in parenthesis is using $g(x, x)$ from the experimental U_0 profile. A great sensitivity to U_0'' is seen, making accurate calculation of γ very problematical. However, the predictions are at least of the correct order of magnitude, which is not a trivial result.

The actual probability distribution is shown in Fig. 31 for the Bermuda experiment and in Fig. 32 for the SD experiment. It is seen that the rays in the partially saturated region have close to a Rayleigh distribution, while the rays in the unsaturated region (late upper and lower in the SD experiment) clearly depart from

TABLE II
OBSERVED MOMENTS

Experiment γ	n	Observed $\langle I^n \rangle$	Rayleigh	Predicted
AFAR 0.23	1	1.0	1	1.0
	2	2.47	2	2.47
	3	11	6	10
	4	74	24	57
Bermuda 0.13	1	1.0	1	1.0
	2	2.26	2	2.26
	3	8.1	6	8.3
	4	38	24	43
	5	220	120	280
San Diego 0.10 ± 0.03	1	1.0	1	1.0
	2	$2.2 \pm .05$	2	2.2
	3	7.9 ± 0.7	6	7.8 ± 0.5

The experimental value of γ is calculated from the experimental second moment of intensity. The Predicted column is obtained from this γ and (67).

TABLE III
CALCULATED RESULTS

Quantity (γ)	AFAR	Bermuda	San Diego
Integral over j of homogeneous ray with same Λ, Φ	0.34	0.31	0.58
Summation over j of homogeneous ray with same Λ, Φ	0.18 (0.25)	0.10 (0.40)	0.28 (0.24)
Integral over j of curved ray	0.25 (0.06)	0.67 (0.23)	0.21 (0.17)
Summation over j of curved ray	0.19 (0.05)	—	0.06 (0.15)
Experiment	0.23	0.13	0.10 ± 0.03

Rayleigh as expected. Neither experiment has enough data to look at the non-Rayleigh tail of the distribution.

The probability distribution for AFAR (Figs. 33 and 34) shows a tail significantly above the Rayleigh expectation, in agreement with predictions as shown in Tables II and III. The curves are K distributions [57], which have moments to first order given by (67).

VIII. PHASE AND LOG-INTENSITY STATISTICS

The foregoing sections covering various moments have only touched a small part of the information contained in the full statistics of the propagating wave field. A good example of information *not* contained in the small number of results already presented is the statistical properties of received phase and log intensity. These two quantities comprise probably the most important practical information existing in the wavefield, for both communication and detection of signal in the presence of additive noise are often done by algorithms depending on phase, with sensitivity to noise measured most appropriately in terms of log intensity. In order to derive the statistics of phase and log intensity, we need a fuller understanding of the complex phasor behavior than is provided by the second and fourth moments. Fortunately such an understanding does exist to some extent; it is tied to the Λ – Φ diagram (Fig. 12).

A. Complex Phasor Behavior in Time

It will be useful to consider the behavior of the complex phasor as a function of time under the influence of internal waves. Fig.

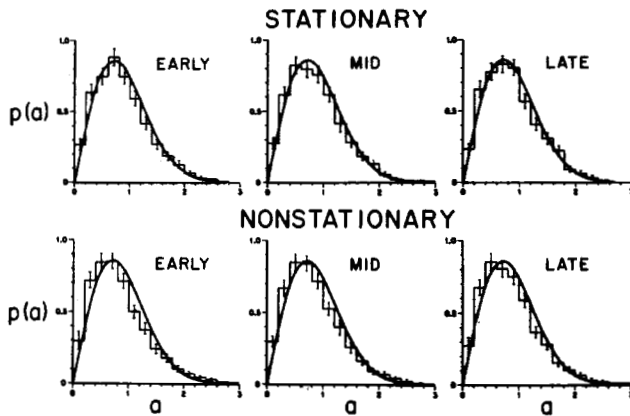


Fig. 31. Histograms of amplitude for the Bermuda experiment [32]. The solid curve in each is a Rayleigh distribution.

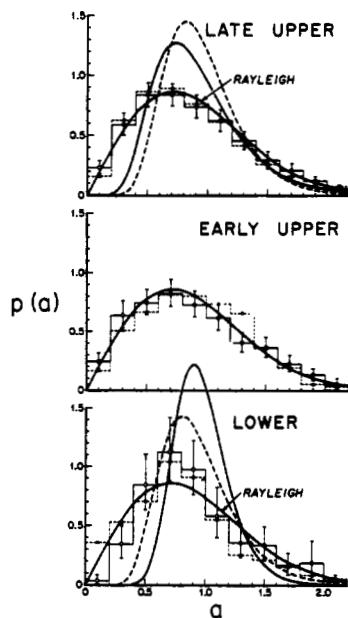


Fig. 32. Histogram of amplitude for the SD experiment [33]. The log-normal predictions of the unsaturated region with parameters calculated from environmental data are shown in the cases where unsaturated behavior is expected. The Rayleigh distribution predicted for the early upper ray is displayed for all three rays.

35 shows the phasor behavior for three experiments that occupy roughly the three important regions of the Λ - Φ diagram. The transition from geometrical optics (small intensity fluctuations) through partial saturation to full saturation is evident in the shift from a phasor moving predominantly in the tangential direction to a two-dimensional random walk. The tangential motion in partial saturation does not prevent the intensity probability distribution from being nearly Rayleigh (see Fig. 34). This tangential motion can be evaluated quantitatively by measuring the angle between the derivative of Ψ and Ψ itself. That is,

$$\phi = \arg [\Psi(\Delta t) - \Psi(0)] - \arg [\Psi(0)]. \quad (120)$$

The distribution of ϕ in the AFAR experiment is shown in Fig. 36, and a clear peaking near 90° (and 270°) is seen, indicating tangential motion. The figure also shows the completely different distribution one would obtain from a two-dimensional random walk. The different experimental curves arise from the fact that a finite Δt is not a perfect evaluation of $\partial_t \Psi$. The theoretical curves arise from a Monte Carlo simulation in which $\Psi(0)$ is chosen from a Rayleigh distribution and $\Psi(\Delta t)$ is generated from

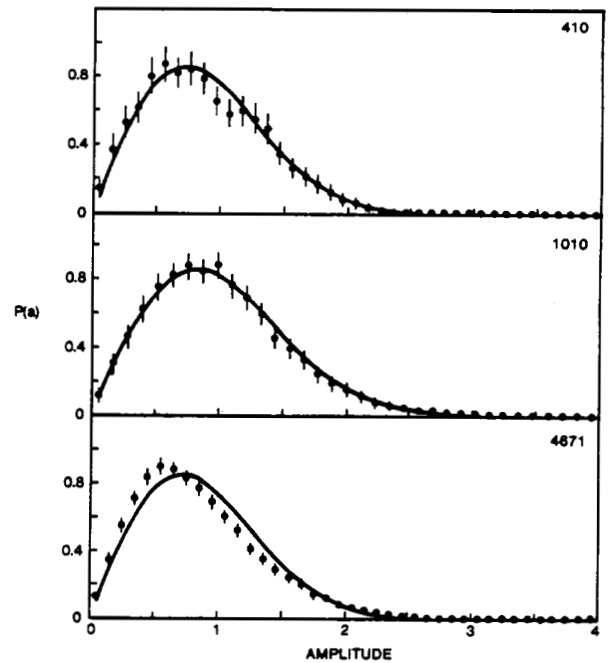


Fig. 33. Histograms of amplitude for the AFAR experiment [24] at three acoustic frequencies. The Rayleigh distribution is also shown.

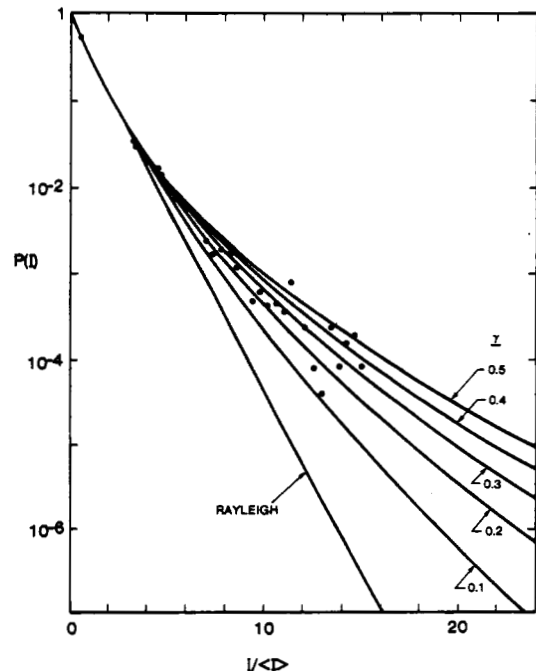


Fig. 34. Histograms of intensity for the AFAR experiment [24] at 4671 Hz (same data as Fig. 33). The corrections to Rayleigh statistics are represented by K distributions [57] chosen so that higher intensity moments match the path integral results [67] to first order.

$$\Psi(\Delta t) = e^{i\phi} \left[X + iY + \Psi(0) \exp \left(-(\nu\Delta t)^2/2 \right) \right] \quad (121)$$

with ϕ , X , and Y being Gaussianly distributed with variances $(\nu\Delta t)^2$, $(\nu\Delta t)^2/2$, and $(\nu\Delta t)^2/2$, where ν and ν' were calculated from environmental parameters. The above formula follows [24] from the picture of partial saturation embodied in (82). If the process were fully saturated so that $\nu' = \nu$ and $\phi = 0$ in (121), then the fully saturated curves shown in Fig. 36 would apply, which are clearly in error. Thus our understanding of partial saturation is quantitatively correct.

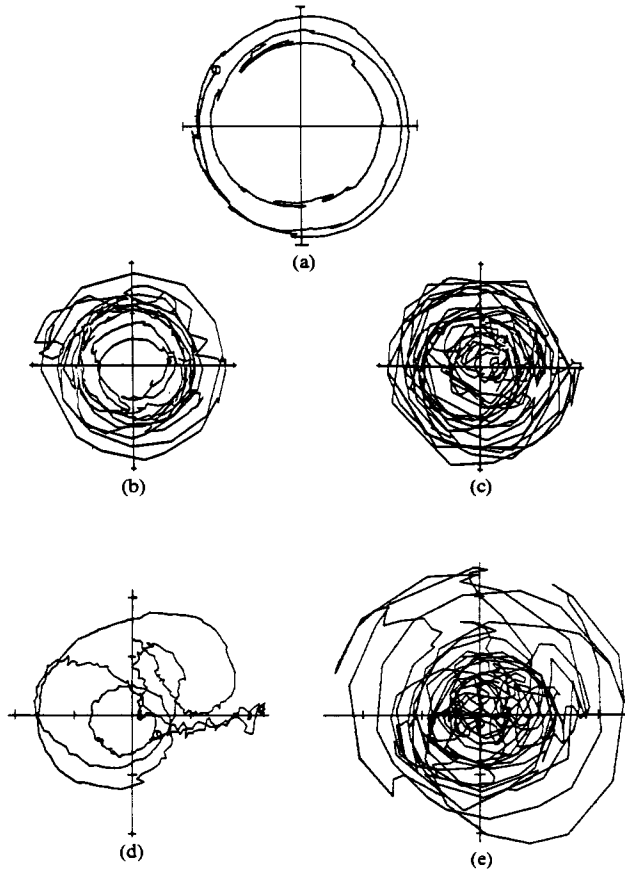


Fig. 35. Sample experimental phasors in ocean acoustics. (a) Geometrical optics from a separate experiment at AFAR (2800 Hz, 5 km). (b) Boundary between geometrical optics and partial saturation from the Cobb experiment (2 kHz, 18 km). (c) Cobb at 4 kHz. (d) Partial saturation from AFAR (1010 Hz, 35 km). (e) AFAR at 4671 Hz.

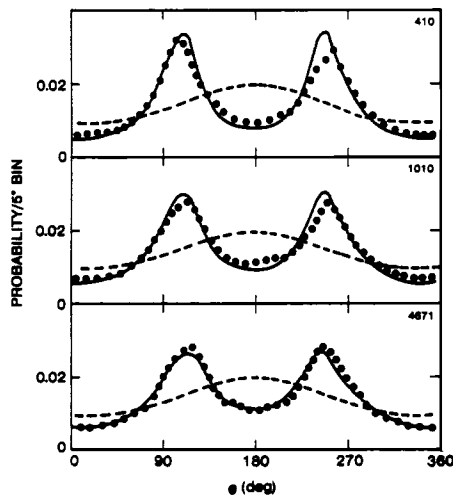


Fig. 36. Distribution of angle between the derivative of $\Psi(t)$ and $\Psi(t)$ itself, at three acoustic frequencies from the AFAR experiment. The closed circles are experimental data. The solid curve is a Monte Carlo simulation of the expected distribution in the partially saturated region with ν and ν' taken from Table I. The dashed curve is the prediction for full saturation, which clearly disagrees with the data.

B. The Unsaturated Region

The Cobb Seamount experiment [69] involved data at 4 and 8 kHz transmitted over 18 km between a source and a receiver that were both below a kilometer in depth. At that depth, the measured internal-wave strength was very weak, as expected, and as a

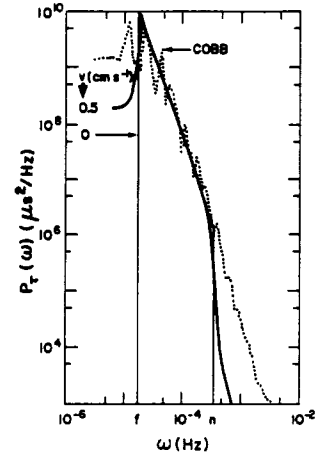


Fig. 37. Travel-time (phase) spectrum for 4-kHz acoustic transmission at Cobb Seamount compared with the geometrical optics prediction from internal waves.

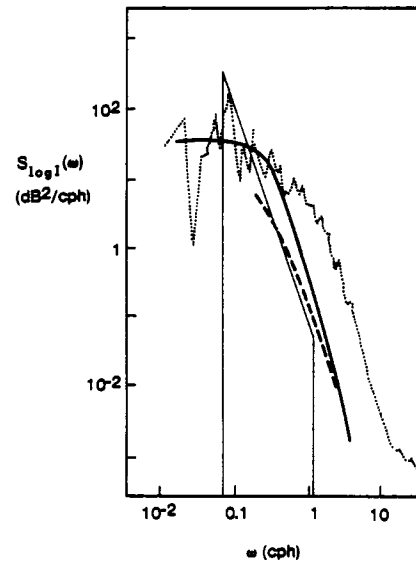


Fig. 38. Log-intensity spectrum for 4-kHz acoustic transmission at Cobb. The band-limited ω^{-3} spectrum is an approximation to the geometrical-optics prediction. The solid curve qualitatively includes the effect of vertical advection of internal waves [34]. The dashed curve [74] includes an approximate correction for multiple scattering. Disagreement at high frequency between theory and experiment is substantial.

result, the calculation of Λ and Φ puts the experiment quite close to the boundary between the unsaturated and partially saturated regions [34]. In geometrical optics one expects a one-to-one correspondence between the observed phase and log-intensity spectra, and the spectra of internal waves, except that the weighting of vertical mode number is toward the low j for phase and toward very high j (on the order of $j \approx 70$) for log intensity [70]. Since the spectrum of internal waves factorizes in j and ω , both phase and log intensity might be expected to have the same spectrum. Fig. 37 shows the Cobb phase spectrum, with the geometrical optics prediction [34] in excellent agreement within the internal-wave band. Fig. 38 shows the log-intensity spectrum, whose total variance as well as high-frequency level are far above the prediction. This major disagreement has prompted a number of attempts at explanation. Unni and Kaufman [71] considered the addition of microstructure fluctuations in the ocean, but used a microstructure level above the observations [72]. Ewart [73] suggested that fluctuations with scales comparable to the acoustic wavelength are responsible, but could not make a quantitative

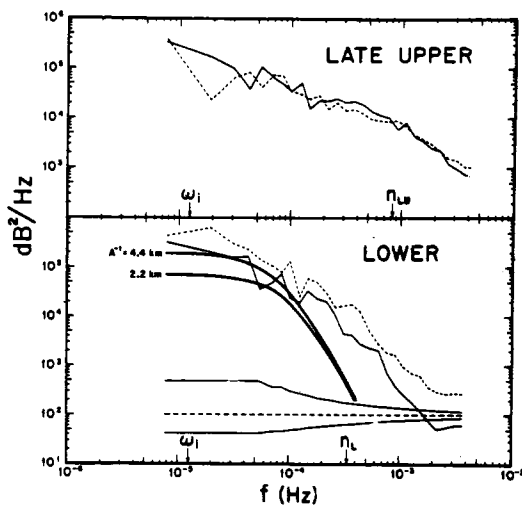


Fig. 39. Log-intensity spectra for the SD experiment. The quantity $A^{-1}(x) = g(x, x)$. The heavy solid curves are from a calculation based on [34]. The 95-percent confidence limits relative to 10^2 are given at the bottom (light solid).

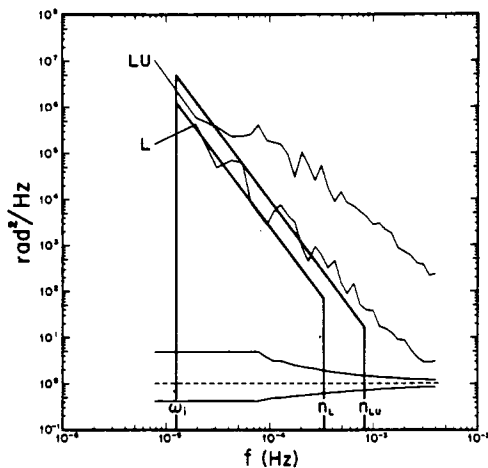


Fig. 40. Spectra of phase difference between two receivers separated vertically by 30.5 m in the SD experiment. Theoretical predictions are from geometrical optics. Confidence limits as in Fig. 39.

comparison with the data. Flatté, Leung, and Lee [34] noted that the internal-wave spectrum will not factorize if the small-vertical-scale waves are advected by the more energetic large-vertical-scale waves. They made a simple qualitative model of the effect, and did show a substantial enhancement in the high-frequency intensity level, but did not achieve agreement with the observed spectrum near the buoyancy frequency (see Fig. 38). It was shown in [34] that the low-frequency end of the spectrum is likely to be sensitive to U_0'' . Desaubies [72] emphasized the qualitative nature of the models in [34] and [71] but offered no solution to the high-frequency discrepancy. Ewart, Macaskill, and Uscinski [74] suggest that Cobb is close enough to the saturation region for there to be a significant correction to the geometrical optics approximation. Their calculation of the effect, using a modification of Shishov's method (Section IV-C) does not give any enhancement in the variance of intensity over the geometrical optics result, and their enhancement of the high-frequency end is not better than that of [34] (see Fig. 38).

The SD experiment's observation of log-intensity spectrum for rays that are expected to be in the unsaturated region shows the same high-frequency discrepancy as that seen at Cobb (see Fig.

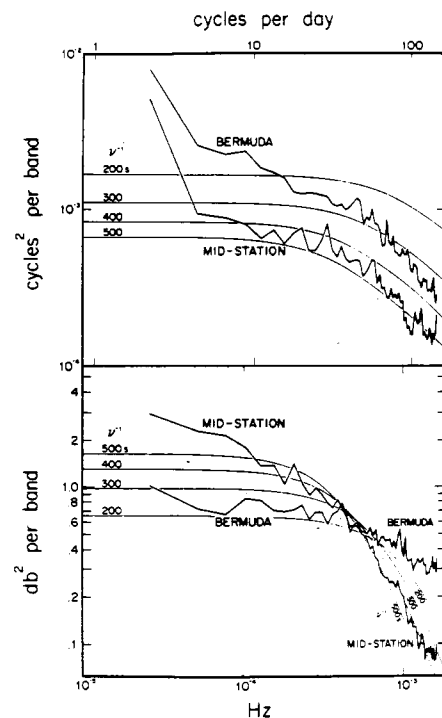


Fig. 41. Spectra of phase difference (over a 5-min sampling interval) and log intensity for the MIMI experiment [24]. Reference band is 0.915 cycle/day. The theoretical curves are from (80) and (81).

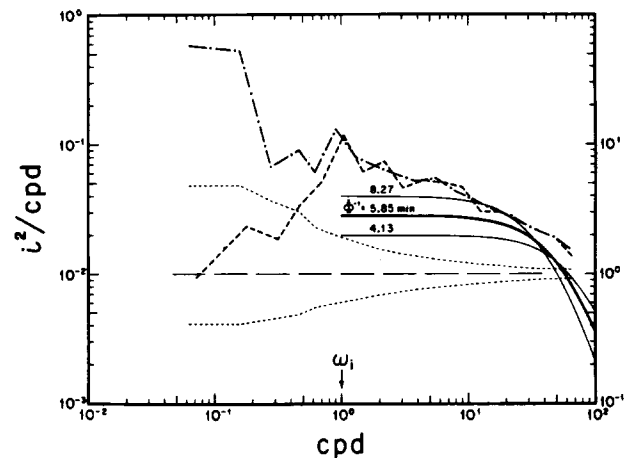


Fig. 42. Log-intensity spectra for the Bermuda experiment [32]. The theoretical curves are from (81) with $\nu = \phi$ as given. Confidence limits as in Fig. 22.

39). The SD experiment could not measure phase because of mooring motion, but the two vertically separated hydrophones allowed the measurement of the spectrum of phase difference, which should be intermediate between phase and log intensity in terms of which j value dominates the observation (typically $j \approx 10$).

Fig. 40 shows that the discrepancy at high frequency is there in the phase-difference spectrum, but not to as high a degree as in the log-intensity spectrum. Any explanation of the log-intensity discrepancy should simultaneously show agreement with the phase-difference spectrum.

C. The Fully Saturated Region

The phase and log-intensity spectra in full saturation should coincide with (80) and (81) where ν is calculated from (79). These empirical spectra are shown in comparison with the MIMI ex-

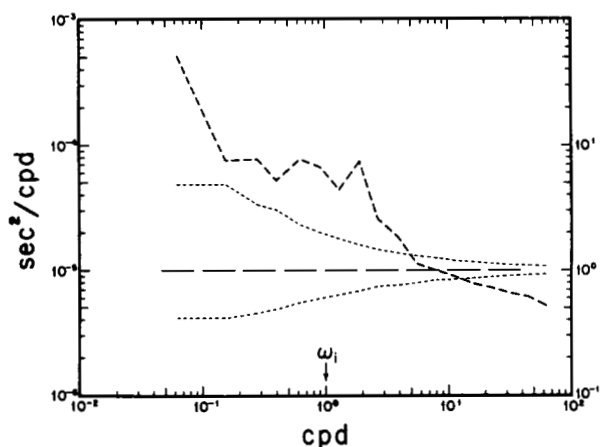


Fig. 43. Spectrum of difference in travel time between the middle and late rays of the Bermuda experiment [32]. Confidence limits as in Fig. 22.

periment in Fig. 41; agreement is seen except at the low-frequency end of the phase spectrum, where coherent action of tides and other long-term phenomena might be expected to have influence.

The other fully saturated experiment (Bermuda) did not have the sampling rate to show the high-frequency end of the phase and log-intensity spectrum. Fig. 42 shows the log-intensity spectrum and again the observed low-frequency level is somewhat high. The Bermuda experiment was unable to directly measure phase or absolute travel time, but travel-time difference between two rays was measured. However, since each pulse spanned somewhat greater than a frequency coherence interval (Fig. 27), the interpretation of this travel-time difference spectrum is somewhat questionable. Fig. 43 shows this spectrum with a theoretical curve calculated assuming no effect of frequency decoherence. In general, agreement in the fully saturated region is good, but more than one long-term experiment like MIMI would be desirable.

D. The Partially Saturated Region

The idea that the phase spectrum in the partially saturated region is approximately the sum of contributions from the geometrical optics phase and the addition of microrays, as represented in (84) is given a striking test in Figs. 44 and 45. The agreement is excellent except for a theoretical overestimate for frequencies near ω_i , which is understandable qualitatively since in the fully saturated region, the whole geometrical optics contribution should disappear, and AFAR is not too far from full saturation. The clear observation of a change in behavior at the buoyancy frequency for 4672-Hz data and the accompanying theoretical agreement indicates again that partial saturation is quantitatively understood.

The log-intensity spectra at AFAR are shown in Fig. 46 compared to (81) with ν replaced by ν' . The agreement at all three frequencies is excellent. A low-frequency excess in the observations at 4672 Hz is the only significant discrepancy. Thus both the phase and log intensity in the partially saturated region have verified the picture represented by (82).

IX. CONCLUSION

Wave-propagation experiments in the ocean have spanned the regimes of WPRM from unsaturated geometrical optics through partial saturation to the fully saturated region. Frequencies from 200 to 8000 Hz have been transmitted over ranges from 18 to 1250 km. In these regimes, it has been determined that the

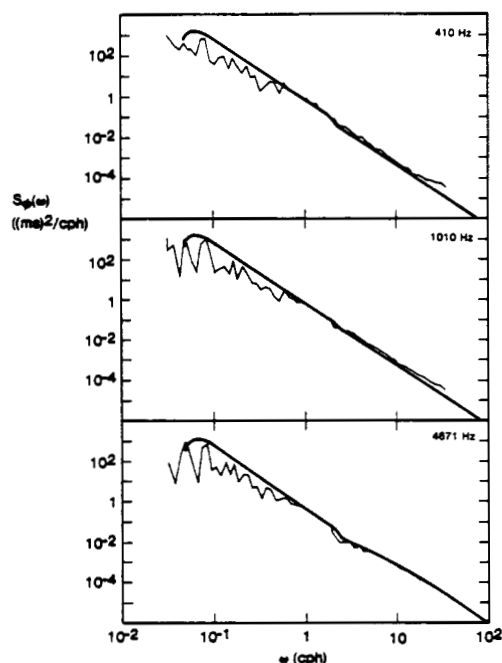


Fig. 44. Travel-time (phase) spectra for three frequencies at AFAR [24]. The heavy curve is the prediction of (84) from environmental measurements.

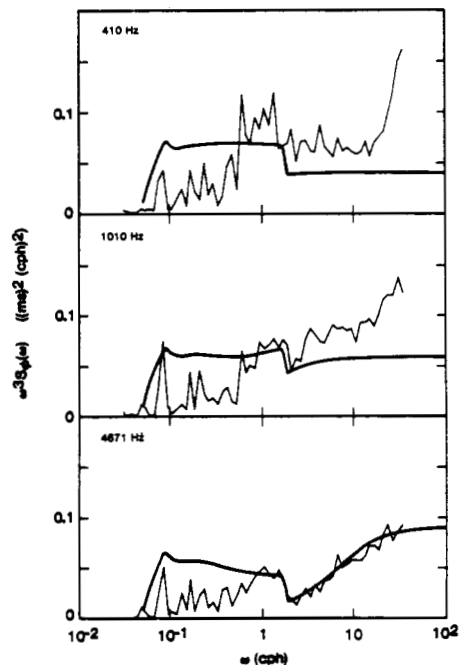


Fig. 45. Variance-preserving travel-time (phase) spectra from AFAR. This figure is the same as Fig. 44 but plotted on a linear scale such that equal areas have equal variance. The change from the geometrical-optics contribution at low frequencies to the microray interference contribution is seen clearly at the buoyancy frequency (≈ 1.8 cycles/h).

random field of internal waves is the dominant source of transmission fluctuations, and that the deterministic ocean sound channel has a major effect on the type of fluctuations observed. Particularly for the saturated regions, the use of path-integral techniques has led to quantitative and satisfactory agreement with second-moment functions and intensity correlations of time, frequency, and vertical separation, including the behavior of pulse propagation. Higher moments of intensity show the expected departure from Rayleigh statistics. An understanding of

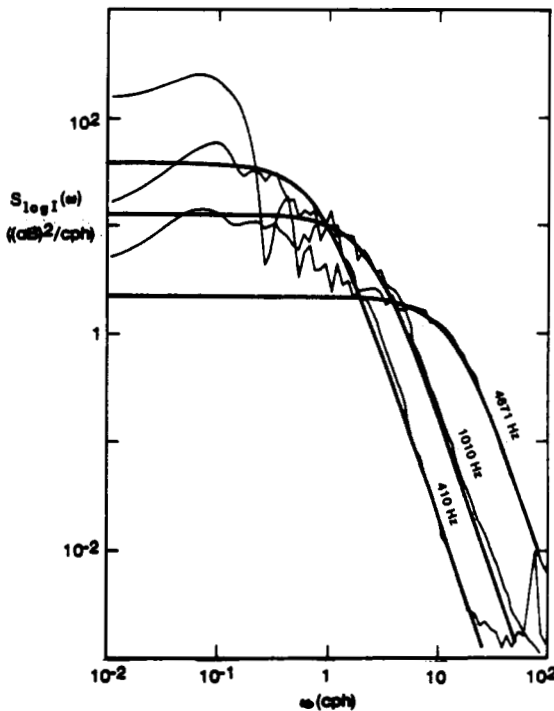


Fig. 46. Log-intensity spectra for three frequencies at AFAR. The theoretical (smooth) curves are from (81) and ν' from Table I.

the behavior of the complex phasor in the saturated region has led to successful comparisons of phase and log-intensity spectra.

These major successes may be applicable to other examples of WPRM, particular those that exhibit a k^{-2} spectrum and/or a significant deterministic wavespeed background to the random fluctuations. They certainly pave the way for the use of sound transmission as a probe of the ocean internal-wave field on a continuous monitoring basis [75], [76].

Unsolved problems in the theory of ocean acoustic fluctuations from internal waves center on the inadequacy of the quadratic approximation to the behavior of ray tubes. This approximation can break down due to the finiteness of the Fresnel-zone radius (of order 20–200 m in typical ocean cases), and the breakdown is influenced by several factors: first, the presence of a nearby caustic; second, rapid changes in the deterministic sound channel versus depth, such as in a surface duct; third, experimental uncertainty in the sound-channel profile, particularly due to the inevitable ambiguity between deterministic and random behavior that always exists in the presence of a “red” spectrum. The theory is not adequate at very low frequencies (below 100 Hz, typically) due to the breakdown of the Markov approximation because of the effects of anisotropy and inhomogeneity, but an accurate measure of the breakdown frequency is available. Finally, the boundaries between the saturated and unsaturated regions are not completely understood as yet.

As the acoustic frequency of experiments is raised above 10 kHz, the scale of the ocean structure will decrease to an extent that internal-wave dominance will probably give way to effects of microstructure, whose character is substantially unknown at present.

A wide variety of future directions in research have been opened up by the recent progress described in this review. Engineering applications in the form of sonar systems are myriad, and the use of acoustics to monitor internal waves is definitely possible. Experimental information of horizontal correlations is sorely needed as is further information on vertical correlations.

This information could be used to test present ideas about the horizontal isotropy and spectral character of the internal-wave field. Finally, theoretical progress on the problems described in the above two paragraphs will require substantial effort, including comparison with experiment.

APPENDIX I INTENSITY CORRELATION FUNCTION $K(\Delta t)$

From (64) we see that $K(\Delta t)$ is calculable from a four-dimensional path integral: that is, a fourth moment of Ψ . By changing variables, this four-dimensional integral can be reduced to a two-dimensional one where the variables are path separations. The method of evaluation will only be sketched here. The form of $f(\Delta z, z, \vartheta)$ in (35) is crucial to the evaluation; by use of (36) and the careful choice of when to approximate the logarithm in (36) by a constant so that $f(\Delta z \dots)$ is a quadratic, the path integral reduces to

$$K(\Delta t) = N \int d^2 \text{paths} \exp \left\{ i q_0 \int [\partial_x \eta \partial_x \xi - U_0''(x) \xi \eta] dx \right\} \cdot \exp \left\{ - \int [H \eta^2 + J \xi^2] dx \right\} \quad (\text{A1})$$

where $\eta(x)$ and $\xi(x)$ are the two paths, and

$$H = \frac{q^2 \langle \mu^2 \rangle L_P}{L_V^2} \ln \Phi \quad (\text{A2})$$

$$J = \frac{q^2 \langle \mu^2 \rangle L_P \ln \beta}{2 L_V^2} \{ \omega^2 \} (\Delta t)^2 \quad (\text{A3})$$

$$\beta = \max \{ e, 1/(2 \Lambda \Phi \ln \Phi) \} \quad (\text{A4})$$

$$\{ \omega^2 \} = \int \{ \tilde{f}(\omega, \vartheta, z) \omega^2 \} d\omega. \quad (\text{A5})$$

Note that $\langle \mu^2 \rangle$, L_P , L_V , and $\{ \omega^2 \}$ are all functions of x , and that (A1) is a quadratic path integral since η and ξ appear in powers up to the square.

The evaluation of this path integral can be carried out by means of Fredholm determinants, and the result is the solution of an ordinary, matrix, differential equation

$$\left[(\partial_{xx} + U_0'') \begin{pmatrix} 0 & 1 \\ 1 & 0 \end{pmatrix} - \frac{2i}{q} \begin{pmatrix} H & 0 \\ 0 & J \end{pmatrix} \right] M(x, \Delta t) = 0 \quad (\text{A6})$$

with initial conditions $M(0, \Delta t) = 0$; $M'(0, \Delta t) = I$ where I is the identity. Then

$$K(\Delta t) = \left\{ \frac{\det M(R, 0)}{\det M(R, \Delta t)} \right\}^{1/2}. \quad (\text{A7})$$

It is useful to note that we may multiply the HJ matrix by any two-by-two diagonal matrix which satisfies the condition $M_{22} = 1/M_{11}$ without affecting the final answer. Thus we may recast (A6) as

$$\left[(\partial_{xx} + U_0'') \begin{pmatrix} 0 & 1 \\ 1 & 0 \end{pmatrix} + \frac{\langle \mu^2 \rangle L_P}{L_V^2} \alpha \begin{pmatrix} 1 & 0 \\ 0 & -\{ \omega^2 \} / \omega_i^2 \end{pmatrix} \right] \cdot M(x, \alpha) = 0 \quad (\text{A8})$$

$$\alpha = q \omega_i \Delta t \{ 2 \ln \beta \ln \Phi \}^{1/2} \quad (\text{A9})$$

and (A8) may be solved as a function of α for a particular ray.

Note that (A8) is a completely real equation, and therefore corresponds to two coupled ordinary differential equations. Note

also that the sign of the $\mu^2 L_P / L_V^2$ term is arbitrary, since one can let $M_{11} \rightarrow -M_{11}$ in the transforming equation.

The only appearance of acoustic wavenumber q and time delay Δt is within the expression for α . The dependence on Δt is simple, but q is also present implicitly in β and Φ , though only in a logarithm or a log-log expression. Thus there is a slightly nonlinear acoustic frequency dependence in α . The agreement of the calculated scaling with experiment is shown in Figs. 24 and 25.

A number of special solutions for $K(\Delta t)$ are given in [24]. In a realistic experimental situation (A8) is solved numerically.

APPENDIX II

MICROPATH BANDWIDTH FUNCTION $Q(\Delta\sigma)$

From (86) we see that $Q(\Delta\sigma)$ is calculable from a two-dimensional path integral, which, upon a change of variable, can be reduced to one dimension

$$N \int d\text{path} \exp \left[-\frac{i\sigma^2}{2C_0\Delta\sigma} \int_0^R [(\partial_x \eta)^2 - U_0'' \eta^2] dx - \int 2q^2 \langle \mu^2 \rangle L_P f(\eta, \vartheta, z) dx \right] \quad (\text{A10})$$

where $\eta(x)$ is the path, and where the normalization is obtained by dividing by the same integral with $\mu = 0$. The evaluation takes the form of a quadratic path integral once $f(\eta, \vartheta, z)$ is approximated, and the solution for Q takes the form of an ordinary differential equation

$$(\partial_{xx} + U_0'')S(x, \Delta\sigma) + i \frac{q \langle \mu^2 \rangle L_P \Delta\sigma}{L_V^2 \sigma} \ln \Phi S(x, \Delta\sigma) = 0 \quad (\text{A11})$$

with initial conditions $S(0, \Delta\sigma) = 0$, $S'(0, \Delta\sigma) = 1$. Then

$$Q(\Delta\sigma) = \{S(R, 0)/S(R, \Delta\sigma)\}^{1/2}. \quad (\text{A12})$$

A number of special solutions for $Q(\Delta\sigma)$ are given in [24]. In realistic experimental situations (A11) is solved numerically.

ACKNOWLEDGMENT

The elaboration of the path-integral theory in application to ocean acoustics, some of which has been presented here for the first time, has been carried out in close collaboration with R. Dashen, who, however, deserves no blame for any errors. The author is grateful to F. Henyey, M. McKisic, and P. Worcester for helpful comments on the first draft, and to S. Reynolds for assistance in a number of calculations. Particular thanks go to B. Buehler who provided much of the AFAR data prior to publication, and to P. Maciejewski who did much of the AFAR data reduction.

REFERENCES

- [1] I. Newton, *Opticks*. New York: Dover, 1952, p. 110.
- [2] P. G. Bergmann, "Propagation of radiation in a medium with random inhomogeneities," *Phys. Rev.*, vol. 70, p. 486, 1946.
- [3] V. A. Krasilnikov, "Dokl. Akad. Nauk. SSSR," vol. 47, p. 482, 1945.
- [4] D. Mintzer, "Wave propagation in a randomly inhomogeneous medium," *J. Acoust. Soc. Amer.*, vol. 25, pp. 922-927, 1953.
- [5] V. I. Tatarskii, "The Effects of the Turbulent Atmosphere on Wave Propagation." Israel Program for Scientific Translation: Jerusalem, Israel, 1971.
- [6] A. M. Prokhorov, F. V. Bunkin, K. S. Gochelashvili, and V. I. Shishov, "Laser irradiance propagation in turbulent media," *Proc. IEEE*, vol. 63, pp. 790-811, 1975.
- [7] A. Ishimaru, "Theory and application of wave propagation and scattering in random media," *Proc. IEEE*, vol. 65, pp. 1030-1061, 1977.
- [8] R. L. Fante, "Electromagnetic beam propagation in turbulent media: An update," *Proc. IEEE*, vol. 68, pp. 1424-1443, 1980.
- [9] V. I. Tatarskii and V. U. Zavorotnyi, "Strong fluctuations in light propagation in a randomly inhomogeneous medium," *Prog. Opt.*, vol. 18, pp. 204-256, 1980.
- [10] J. W. Strohbehn, Ed. *Laser Beam Propagation in the Atmosphere*. Berlin, Germany: Springer, 1978.
- [11] M. Leontovich and V. Fok, "Solution of the problem of propagation of electromagnetic waves along the earth's surface by the parabolic equation method," *Zh. Eksp. Teor. Fiz.*, vol. 16, pp. 557-573, 1946.
- [12] C. L. Rino and E. J. Fremouw, "The angle dependence of single scattered wavefields," *J. Atmos. Terr. Phys.*, vol. 39, pp. 859-868, 1977.
- [13] C. L. Rino, R. C. Livingston, and S. J. Matthews, "Evidence for sheet-like auroral ionospheric irregularities," *Geophys. Res. Lett.*, vol. 5, pp. 1039-1042, 1978.
- [14] R. P. Mercier, "Diffraction by a screen causing large random phase fluctuations," *Proc. Cambridge Phil. Soc.*, vol. 58, pp. 382-400, 1962.
- [15] R. Woo, F. Yang, and A. Ishimaru, "Structure of density fluctuation near the sun deduced from Pioneer 6 spectral broadening measurements," *Astrophys. J.*, vol. 210, pp. 593-602, 1976.
- [16] R. Woo and K. Armstrong, "Spacecraft radio scattering observations of the power spectrum of electron density fluctuations in the solar wind," *J. Geophys. Res.*, vol. 84, pp. 7288-7296, 1979.
- [17] G. L. Tyler, J. F. Vesecky, M. A. Plume, H. T. Howard, and A. Barnes, "Radio wave scattering observations of the solar corona: First-order measurements of expansion velocity and turbulence spectrum using Viking and Mariner 10 spacecraft," *Astrophys. J.*, vol. 249, pp. 318-332, 1981.
- [18] R. Woo and F. Yang, "Measurements of electron density irregularities deduced from Jupiter by Pioneer 10," *J. Geophys. Res.*, vol. 81, pp. 3417-3422, 1976.
- [19] ———, "Measurements of magnetic field orientation in the jovian ionosphere deduced from Pioneer 10 and 11 scintillation measurements," *J. Geophys. Res.*, vol. 83, pp. 5245-5255, 1978.
- [20] R. Woo and A. Ishimaru, "Radio scintillation during occultations by turbulent planetary atmospheres," *Radio Sci.*, vol. 15, pp. 695-703, 1980.
- [21] R. Woo, J. Armstrong, and A. Ishimaru, "Radio occultation measurements of turbulence in the Venus atmosphere by Pioneer Venus," *J. Geophys. Res.*, vol. 85, pp. 8031-8038, 1980.
- [22] B. S. Haugstad, "Turbulence in planetary occultations," *Icarus*, vol. 35, pp. 121-138, 410-435, 1978.
- [23] C. Garrett and W. H. Munk, "Spacetime scales of internal waves: A progress report," *J. Geophys. Res.*, vol. 80, pp. 291-297, 1975.
- [24] S. M. Flatté, R. Dashen, W. H. Munk, K. M. Watson, and F. Zachariasen, *Sound Transmission Through a Fluctuating Ocean*. New York: Cambridge Univ. Press, 1979.
- [25] W. H. Munk and F. Zachariasen, "Sound propagation through a fluctuating ocean—Theory and observation," *J. Acoust. Soc. Amer.*, vol. 59, pp. 818-838, 1976.
- [26] F. D. Tappert and R. H. Hardin, in *Proc. 8th Int. Congress on Acoustics*, vol. II. London: Goldcrest, 1974, p. 452.
- [27] F. D. Tappert, "Parabolic equation method in underwater acoustics," *J. Acoust. Soc. Amer.*, vol. 55, p. S34A, 1974.
- [28] S. M. Flatté and F. D. Tappert, "Calculation of the effect of internal waves on oceanic sound transmission," *J. Acoust. Soc. Amer.*, vol. 58, pp. 1151-1159, 1975.
- [29] W. R. Hamilton, *The Mathematical Papers of Sir William Rowan Hamilton vols. I, II and III*. Cambridge, England: Cambridge Univ. Press, 1931.
- [30] R. P. Feynman and H. Hibbs, *Quantum Mechanics and Path Integrals*. New York: McGraw-Hill, 1965.
- [31] R. Dashen, "Path integrals for waves in random media," SRI Tech. Rep., JSR 76-1, or *J. Math. Phys.*, vol. 20, pp. 894-920, 1979.
- [32] J. L. Spiesberger and P. F. Worcester, "Fluctuations of resolved acoustic multipaths at long range in the ocean," *J. Acoustic. Soc. Amer.*, vol. 70, pp. 565-576, 1981.
- [33] P. F. Worcester, G. O. Williams, and S. M. Flatté, "Fluctuations of resolved acoustic multipaths at short range in the ocean," *J. Acoust. Soc. Amer.*, vol. 70, 825-840, 1981.
- [34] S. M. Flatté, R. Leung, and S. Y. Lee, "Frequency spectra of acoustic fluctuations caused by oceanic internal waves and other fine structure," *J. Acoust. Soc. Amer.*, vol. 68, pp. 1773-1779, 1980.
- [35] M. E. Gracheva and A. S. Gurvich, "Strong fluctuations in the intensity of light propagated through the atmosphere close to the earth," *Radio-phys. Quantum Electron.*, vol. 8, pp. 511-525, 1965.
- [36] K. Furutsu, "Review of the theory of the irradiance distribution function in turbulent media with a particular emphasis on analytical methods," *Radio Sci.*, vol. 14, pp. 287-299, 1979.
- [37] S. Ito and K. Furutsu, "Theoretical analysis of the high-order irradiance moments of light waves observed in turbulent air," *J. Opt. Soc. Amer.*, vol. 72, pp. 760-764, 1982.
- [38] W. C. Meecham, M. T. Tavis, and H. T. Yura, "Born series sums for wave propagation in anisotropic random media," *J. Acoust. Soc. Amer.*, vol. 70, pp. 520-534, 1981.
- [39] B. J. Uscinski, C. Macaskill, and T. E. Ewart, "Intensity fluctuations I-theory," submitted to *J. Acoust. Soc. Amer.*, June 1982.

- [40] R. Mazur and M. J. Beran, "Intensity corrections in a random medium in the neighborhood of a caustic," *J. Acoust. Soc. Amer.*, vol. 72, pp. 1269-1275, 1982.
- [41] M. J. Beran, A. M. Whitman, and S. Frankenthal, "Scattering calculations using the characteristic rays of the coherence function," *J. Acoust. Soc. Amer.*, vol. 71, pp. 1124-1130, 1982.
- [42] C. Macaskill, B. J. Uscinski, and N. Freedman, "Acoustic propagation in the upper sound channel," *J. Acoust. Soc. Amer.*, vol. 72, pp. 1544-1555, 1982.
- [43] M. J. Beran and J. J. McCoy, "Propagation through an anisotropic medium," *J. Math. Phys.*, vol. 15, pp. 1901-1912, 1974.
- [44] ———, "Propagation of radiation from a finite beam of source through an anisotropic random medium," *J. Acoust. Soc. Amer.*, vol. 56, pp. 1667-1672, 1974.
- [45] I. M. Besieris and F. D. Tappert, "Kinetic equation for the quantized motion of a particle in a randomly perturbed potential field," *J. Math. Phys.*, vol. 14, pp. 1829-1836, 1973.
- [46] ———, "Stochastic wave-kinetic theory in the Liouville approximation," *J. Math. Phys.*, vol. 17, pp. 734-743, 1976.
- [47] H. L. Wilson and F. D. Tappert, "Acoustic propagation in random oceans using the radiation transport equation," *J. Acoust. Soc. Amer.*, vol. 66, p. 256, 1979.
- [48] W. M. Ewing and J. L. Worzel, "Long range sound transmission," *Geol. Soc. Amer. Mem.*, vol. 27, part III, pp. 1-35, 1948.
- [49] H. Weinberg, "Application of ray theory to acoustic propagation in horizontally stratified oceans," *J. Acoust. Soc. Amer.*, vol. 58, pp. 97-109, 1975.
- [50] O. M. Phillips, *Dynamics of the Upper Ocean*. Cambridge, England: Cambridge Univ. Press, 1966.
- [51] Y. J. F. Desaubies, "Internal waves near the turning point," *Geophys. Fluid Dyn.*, vol. 2, pp. 143-154, 1973.
- [52] R. Esswein and S. M. Flatté, "Calculation of the phase structure function density from oceanic internal waves," *J. Acoust. Soc. Amer.*, vol. 70, pp. 1387-1396, 1981.
- [53] R. Esswein and S. M. Flatté, "Calculation of the strength and diffraction parameters in oceanic sound transmission," *J. Acoust. Soc. Amer.*, vol. 67, pp. 1523-1531, 1980.
- [54] B. Uscinski, *The Elements of Wave Propagation in a Random Medium*. New York: McGraw Hill, 1977.
- [55] A. Ishimaru, *Wave Propagation and Scattering in Random Media*. New York: Academic Press, 1978.
- [56] S. M. Flatté, D. R. Bernstein, and R. Dashen, "Intensity moments by path integral techniques for wave propagation through random media, with application to sound in the ocean," *Phys. Fluids*, vol. 26, pp. 1701-1713, 1983.
- [57] E. Jakeman and P. N. Pusey, "Significance of K distributions in scattering experiments," *Phys. Rev. Lett.*, vol. 40, pp. 546-550, 1978.
- [58] G. Parry, "Measurement of atmospheric turbulence induced intensity fluctuations in a laser beam," *Opt. Acta*, vol. 28, pp. 715-728, 1981.
- [59] V. I. Shishov, "Strong fluctuations of the intensity of a plane wave propagating in random medium," *Sov. Phys.—JETP*, vol. 34, pp. 744-748, 1972.
- [60] K. S. Gochelashvili and V. I. Shishov, "Saturated fluctuations in the laser radiation intensity in a turbulent medium," *Sov. Phys.—JETP*, vol. 39, pp. 605-609, 1974.
- [61] K. Furutsu, "On the statistical theory of electromagnetic waves in a fluctuating medium," *J. Res. Nat. Bur. Stand.*, vol. 67D, pp. 303, 1963.
- [62] E. A. Novikov, "Functionals and the random-force method in turbulence theory," *Sov. Phys.—JETP*, vol. 20, pp. 1290, 1965.
- [63] V. I. Klyatskin and V. I. Tatarskii, "A new method of successive approximations in the problem of the large-scale inhomogeneities," *Radiophys. Quantum Electron.*, vol. 14, pp. 1100-1111, 1971.
- [64] A. W. Ellinthorpe *et al.*, Naval Underwater Systems Center Tech. Memo. associated with the Joint Oceanographic/Acoustic Experiment, NUSC 4551, 3103-66-77, 4647; 1975-77, New London, CT, 1977.
- [65] B. G. Buehler, "Volume propagation experiments at the Azores fixed acoustic range, Naval Underwater Systems Center," Tech. Rep. 5785, 1979.
- [66] S. M. Flatté, "Spectra of reciprocal transmission: Generalization to the saturated regions," *J. Phys. Ocean.*, vol. 11, pp. 455-466, 1981.
- [67] P. F. Worcester, "Reciprocal acoustic transmission in a midocean environment," *J. Acoust. Soc. Amer.*, vol. 62, pp. 895-905, 1977.
- [68] W. Munk, P. Worcester, and F. Zachariasen, "Scattering of sound by internal-wave currents: The relation to vertical momentum flux," *J. Phys. Ocean.*, vol. 11, pp. 442-454, 1981.
- [69] T. E. Ewart, "Acoustic fluctuations in the open ocean—a measurement using a fixed refracted path," *J. Acoust. Soc. Amer.*, vol. 60, pp. 46-59, 1976.
- [70] Y. J. F. Desaubies, "On the scattering of sound by internal waves in the ocean," *J. Acoust. Soc. Amer.*, vol. 59, pp. 818-838, 1976.
- [71] S. Unni and C. Kaufman, "Acoustic fluctuations due to the temperature fine structure of the ocean," *J. Acoust. Soc. Amer.*, vol. 69, pp. 676-680, 1981.
- [72] Y. Desaubies, "Note on fine structure models in underwater acoustics," *J. Acoust. Soc. Amer.*, vol. 72, pp. 892-895, 1982.
- [73] T. E. Ewart, "A numerical simulation of the effects of oceanic fine structure on acoustic transmission," *J. Acoust. Soc. Amer.*, vol. 67, pp. 496-503, 1980.
- [74] T. E. Ewart, C. Mascaskill, and B. J. Uscinski, "Intensity fluctuations II — Comparison with the Cobb experiments," submitted to *J. Acoust. Soc. Amer.*, June 1982.
- [75] S. M. Flatté, "Sound transmission through internal waves, including internal-wave tomography, in *Proc. Symp. in Honor of Walter Munk's 65th Birthday* (Scripps Institution of Oceanography, La Jolla, CA, 1983).
- [76] ———, "Principles of acoustic tomography of internal waves," in *Proc. IEEE Oceans '83*, 1983.